Thermal and Hydraulic Characterization of Hook-Shaped Fins and Dimples

by

Karim Alrefaey

A Thesis submitted to the
Faculty of Graduate Studies in Partial
Fulfillment of the Requirements for the Degree of

Master of Applied Science

Department of Mechanical Engineering

Lassonde School of Engineering

York University

Toronto, Ontario

April 2025

Abstract

In forced convection, extended surface arrays enhance heat transfer by increasing surface area, promoting fluid mixing, and generating turbulence. Their thermal-hydraulic performance can be modified by introducing tip clearance or adjusting the attack angle. This study quantifies the heat transfer coefficient and pressure drop of GRIPMetal arrays – hook-shaped fins with dimples – under varying tip clearances and attack angles. Experiments with water-cooled GRIPMetal surfaces explored Reynolds numbers (*Re*) from 600 to 12,000, while simulations examined attack angles (α) from 0° to 90°. Results showed that GRIPMetal significantly outperforms smooth surfaces, with Nusselt number (*Nu*) enhancements of 2.4 to 5.7 times higher, despite increased pressure drop. Accounting for the pressure drop penalty, the overall performance factor remained above 1.4. Numerical findings revealed that $\alpha = 22.5°$ improved *Nu* by 44% at $Re = 5000$, and some configurations reduced pressure drop. These results highlight GRIPMetal's potential as a cost-effective heat transfer enhancement method.

Keywords: Forced Convection Enhancement; Thermal-Hydraulic Characterization; Attack Angle; Computational Fluid Dynamics; Liquid Cooling; Extended Surfaces; GRIPMetal; Skiving.

Acknowledgements

I would like to express my deepest gratitude to Prof. Roger Kempers. His insightful guidance, constant support, and continual encouragement have been instrumental to my academic development and have profoundly enriched my educational journey. I am deeply thankful for his belief in my abilities, which has motivated me to grow both professionally and personally, shaping the individual I am today. I am also sincerely grateful to NSERC and NUCAP Industries, particularly John Swift, for their generous funding and support, which have significantly facilitated the completion of this project.

I also extend my heartfelt thanks to my esteemed colleagues and former teaching assistants, Mohamed Hasan and Ahmed Azzam. Their unwavering support and shared expertise have been invaluable to my academic endeavors, and I am sincerely grateful for the collaborative spirit they have created. I am equally appreciative of Ismail Alkomy and Pierre-André Lesbats, whose companionship has brought both joy and resilience to challenging times, making every obstacle feel more manageable.

To my dear friends and second family—Abdalrahman Alsaka, Omar Hammad, Ahmed Shoukry, Omar Elganayny, Abdelrahman Baraka, Ahmed Elgazwy, Abdelhameid Magdy, and Omar Salah—thank you for your enduring friendship, which has left an indelible mark on every aspect of my life. Your presence has provided me with continuous support and countless memories that I will forever cherish. Similarly, I extend my gratitude to my lifelong friends, Mohamed Mokaa,

Khaled Sabry, and Mazen Ali, for their devoted commitment to keeping me a part of their lives.

Most importantly, I am profoundly grateful to my father. Your dedication, strength, and resilience have provided me with an unparalleled role model. Though it is a long journey to produce the hero you are, walking this path in your footsteps is an honor I deeply cherish. To my mother, Manal, thank you for being the constant source of unconditional love and unwavering support that has carried me through life's challenges. Your sacrifices and care have provided me with a foundation for all that I have achieved.

I am also immensely grateful to my siblings—Dr. Basant Alrefaey, Eng. Ahmed Alrefaey, and Sondos Alrefaey. Your love, encouragement, and belief in me have been a cornerstone of my success, and your presence remains a source of strength, no matter the distance that separates us.

Lastly, no words can fully express my gratitude to my wonderful fiancé, Maryam Pirzada. Thank you for your boundless love, care, support, and trust. You have been my faithful companion and best friend when I needed one most, my source of comfort in challenging times, and the home I longed for. Your presence brings joy to my life and a smile to my face. Thank you for being the complementary part of my journey. Thank you for being my solace and my inspiration. Here's to embarking on this new chapter and building a future together, hand in hand.

Table of Contents

Nomenclature

Symbol	**Definition**
A_o	Base surface area of the array
A_s	Array surface area
a	Aspect ratio of the channel
C_h	Spanwise spacing between the hooks within each group
C	Tip clearance
$C_{p,w}$	Water specific heat capacity
C_p	Specific heat capacity
D_h	Hydraulic diameter
E	Voltage
f	Friction factor
f_{D_h}	Hydraulic diameter-based friction factor
f^*_o	Friction factor for the smooth surfaces
f_{avg}	Average coefficient of friction
$f_{o,exp}$	Experimental friction factor for a smooth surface
f_h	Hook height-based friction factor or feature height
f_d	Feature diameter
f_p	Transverse pitch
H	Channel height
h	Hook height
h_{avg}	Average heat transfer coefficient over the surface
I	Current through heater wires

k_{Al}	Thermal conductivity of the Al6061
k	Thermal conductivity or turbulent kinetic energy
L_h	Hook length
L_g	Groove length
L	Length of the channel
L_c	Characteristic length of the arrays
L_d	Developing layer length
Nu	Nusselt number
Nu_{L_c}	Characteristic length-based averaged Nusselt number
Nu^*_o	Nusselt number for the smooth surfaces
Nu_{avg}	Average Nusselt number
$Nu_{o,exp}$	Experimental Nusselt number for a smooth surface
Nu_h	Hook height-based Nusselt number
$Nu_{h,C}$	Hook height-based Nusselt number at the minimum tip clearance
Nu_x	Local Nusselt number
Pr	Prandtl number
p	Pressure
$Q_{in,net}$	Net input power from the heaters
Q_{loss}	Heat lost to the surroundings
Q_{flow}	Volumetric flow rate inside the channel
Q_{water}	Heat gained by water
$Q_{viscous}$	Viscous heating
q_{flux}	Uniform heat flux applied at the base of the strip
Re	Reynolds number
Re^*_o	Equivalent Reynolds number

Re^*	Modified *Re* that establishes a geometric similarity between circular ducts and rectangular channels
$\widetilde{Re}_{\theta t}$	Transition momentum thickness Re
S_L	Streamwise spacing between the hooks within each group
S_T	Spanwise spacing between each group set
St	Stanton number for the finned surfaces
St^*_o	Stanton number for the smooth surfaces
$T_{RTD,x}$	Reading of the RTD at location x
$T_{s,x}$	Array surface temperature at location x
T_{bulk}	Mean water bulk temperature
T_{in}	Water inlet temperature
T_{out}	Water outlet temperature
$T_{w,x}$	Water bulk temperature at location x
T_{amb}	Ambient temperature
$T_{w,in}$	Wall inlet temperature
$T_{w,out}$	Wall outlet temperature
V_{avg}	Area-averaged flow velocity inside the channel
$\boldsymbol{V}$	Velocity vector
W_h	Hook width
W	Width of the channel
α	Attack angle
ΔT_{avg}	Average temperature difference between the heated surface and the bulk water temperature
ΔP	Pressure loss across the test section
ΔT_{LMTD}	Logarithmic mean temperature difference between the wall surface and the bulk fluid temperature

ΔNu_{avg}	Relative change in Nu_{avg}
Δf_{avg}	Relative change in f_{avg}
δ	Distance between the center of the RTDs and the array surface
η_o	Thermal enhancement factor
ε_{Nu_o}	Percentage error between $Nu_{o,exp}$ and correlation predictions
ε_{f_o}	Percentage error between $f_{o,exp}$ and correlation predictions
Φ	Volumetric heat generation rate
γ	Turbulence intermittency
μ_w	Absolute water viscosity
μ	Dynamic viscosity
ρ	Density
ρ_w	Water density
ω	Turbulent kinetic energy specific dissipation rate
ω_F	Uncertainty in a certain variable F

List of Tables

List of Figures

Chapter 1

Introduction

1.1 Enhancement of Convective Heat Transfer

Enhancement of convective heat transfer can improve the thermal performance of cooling systems in various applications (e.g., air conditioners, solar collectors, gas turbine blades, electronic component coolers) and across many industries (e.g., chemical, biomedical, aerospace) [1–3]. Several techniques can be used to achieve this enhancement, including the addition of extended surfaces, surface roughness, fluid additives, microchannels, and porous media, and by using electrostatic or magnetic fields [1,3,4]. Among these methods, the most common is to add extensions such as fins or vortex generators to heat transfer surfaces [5,6] to increase the effective surface area for heat transfer. This method has proven to be a reliable and effective cooling solution for a range of applications, like gas turbine blade cooling, for example.

To enhance the turbine’s output power and efficiency, turbine inlet temperatures have recently been increased. However, due to the temperature limitations of blade materials, advanced cooling techniques are necessary to maintain blade integrity. Internal cooling in modern gas turbines employs various strategies, including the use of protrusions, pin fins, and dimples, as illustrtaed in Fig. 1a. Another application of surface enhancement techniques can be found in IGBT cold plates, which are employed in thermal management when air cooling proves insufficient. In this case, cooling liquid flows through the cold plate, which typically incorporates internal fins to enhance heat transfer from the device or component attached to the plate (see Fig. 1b).

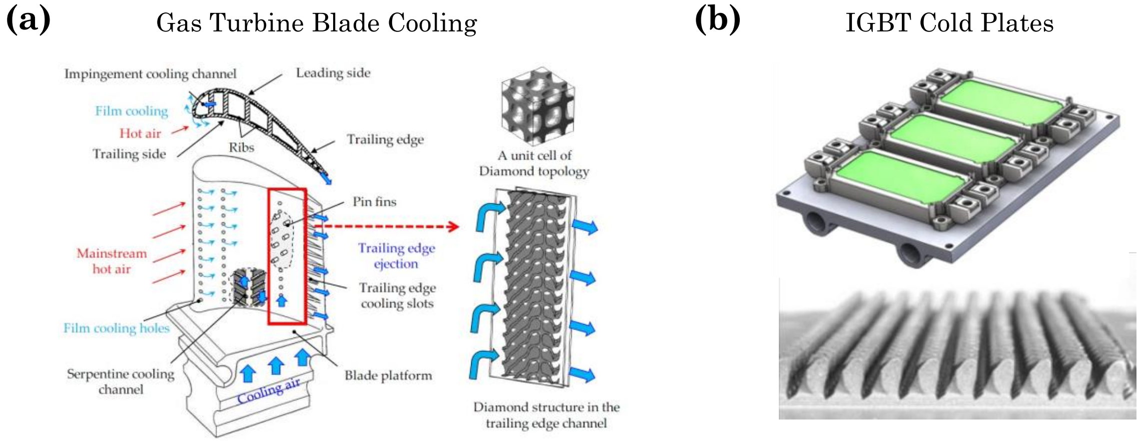
(a) Gas Turbine Blade Cooling

(b) IGBT Cold Plates

Fig. 1. Applications of extended surfaces in forced convective cooling enhancement: (a) gas turbine blade cooling (adapted from Yeranee et al.[7]**) and (b) IGBT cold plates (adapted from MICROCOOL®).**

Many examples of the heat transfer enhancement techniques have been extensively studied in the literature, and they all rely on two key phenomena: increasing the heat transfer surface area and enhancing fluid mixing (typically through flow separation and reattachment, which causes boundary layers to restart) and turbulence, resulting in higher convective heat transfer coefficients (HTC) [5,6,8–10].

The simplest example of extended surfaces is cylindrical pin fins, which can enhance the overall cooling performance of a bare surface by a factor of 1.2 to 1.6, as illustrated in Fig. 2. Introducing dimples to the fins provides a slight improvement in performance [10].

Pin fins are not limited to cylindrical profiles; they can have square [1], or diamond-shaped profiles [11]. Adding grooves to the surface of the pins can further accelerate the flow and enhance mixing, significantly boosting the fins' performance.

As shown in Fig. 2, cylindrical grooved pins outperform standard cylindrical pins, and modifying the pin shape can yield even greater improvements. For instance, the triangular grooved fins exhibit substantially higher performance compared to cylindrical grooved fins [6]. Additionally, various shapes of vortex generators can be employed to achieve further enhancements [8].

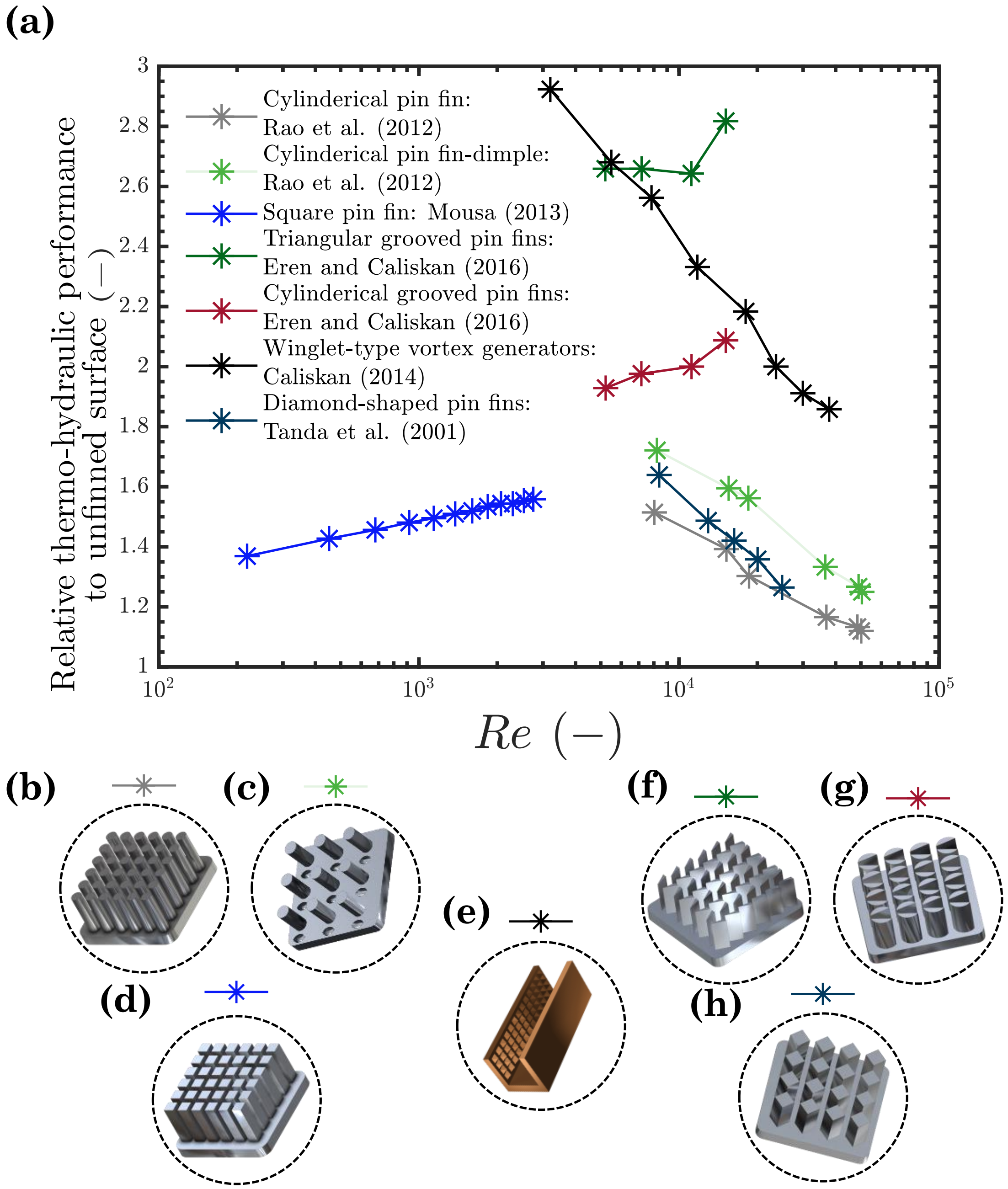

Fig. 2. Examples of surface enhancement techniques: (a) performance of the extended surfaces relative to a bare surface, (b) cylindrical pin fins [10], **(c) cylindrical pin-dimples** [10], **(d) square pins** [1], **(e) winglet vortex generator** [8], **(f) triangular-grooved pins** [6], **(g) cylindrical grooved pins** [6], **and (h) diamond-shaped pins** [11].

1.2 Surface Enhancement Techniques – Challenges and Alternative Solutions

The addition of pin fins or dimples can significantly improve convective heat transfer at a surface, but manufacturing these features can be laborious and costly, especially for miniature geometries. Although simple fins can be economically manufactured, their thermal performance is typically limited. However, increasing their complexity to improve performance can result in higher manufacturing costs. For example, the feasibility of groove and dimple manufacturing largely depends on the required precision because it involves complex processes such as micro-milling, stamping, and pressing [3].

NUCAP Industries has developed a method to create arrays of hook-shaped fins and dimples on metal surfaces (trademarked as GRIPMetal), as shown in Fig. 3. Initially employed to attach brake pad friction material to the backing plate, these arrays have since been applied in various heavy-duty mechanical bonding applications. The arrays are created by a proprietary skiving technique applied to flat metal surfaces, creating hook-shaped protrusions and leaving grooves in their place [12]. This skiving process is simple and robust, and it has been shown to enhance heat transfer rates for both single-phase and two-phase applications [13,14]. Consequently, GRIPMetal arrays hold significant potential for integration into heat exchangers, making them suitable for a wide range of thermal management applications, including HVAC systems, electronics cooling, boilers, gas turbines, and nuclear reactors.

In this regard, this study focuses on testing and characterizing GRIPMetal arrays and evaluating their suitability for forced convective heat transfer applications by comparing their performance with existing surface enhancement techniques reported in the literature. The simplicity and cost-effectiveness of GRIPMetal's manufacturing process make it a promising economical alternative to currently employed heat enhancement methods. The scope of the study includes:

- Characterizing the thermal and hydraulic performance of three types of GRIPMetal arrays.
- Investigating the impact of tip clearance on their their thermal-hydraulic performance.
- Evaluating the overall performance of GRIPMetal arrays.
- Developing correlations to describe the thermal-hydraulic behaviour of the arrays.
- Assessing the effect of varying the attack angle on the arrays' performance.
- Analyzing the flow structure around the arrays to gain insights into their performance.

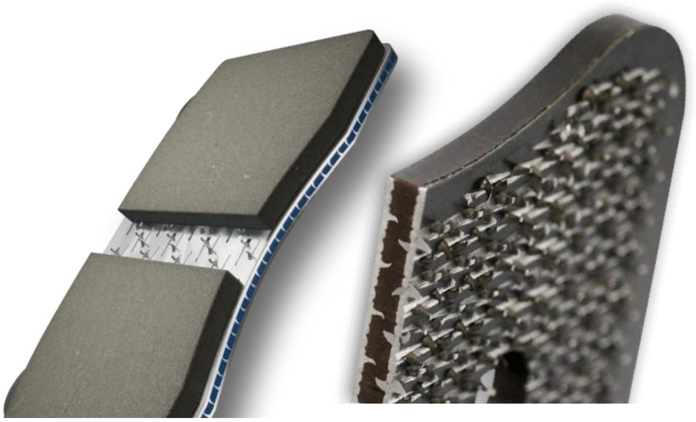

Fig. 3. GRIPMetal arrays manufactured by NUCAP Industries®.

The findings of this study will enhance the understanding of GRIPMetal arrays’ thermo-fluidic performance and the influence of key parameters. These insights can inform further improvements and represent a first step towards optimizing the arrays' performance.

Chapter 2

Literature Review

2.1 Effect of Size, Shape, and Pattern on the Heat Transfer Rate

The focus of recent research is to optimize heat sink designs to achieve improved fluid-geometry interaction, thereby enhancing heat transfer rates [15]. Heat transfer rate is affected by the size, shape, pattern, and flow conditions of extended surfaces, and studies have been conducted to investigate these effects [11,16].

Bilen et al. [5] showed that streamwise spacing has a stronger impact on thermal performance in in-line fin arrays than in staggered arrays. Staggered arrays, however, showed slightly better overall thermal-hydraulic performance when pressure drop is considered. Similarly, Metzger et al. [17] observed a 5-10%

increase in the average Nusselt number, *Nu*, as the streamwise-spacing-to-diameter ratio decreased by 40% for staggered cylindrical pin fins.

The overall performance of pin fins can be improved by changing their shape: Mousa [1] showed that square pins enhance heat transfer more than cylindrical pins due to increased turbulence. Tanda [11] reported an improved thermal performance of diamond-shaped pin fins at lower inter-fin spacings, with staggered fins outperforming the in-line ones at the expense of increased pressure drop.

Enhancing fluid mixing can improve the performance of pin fins. Eren et al. [6] found that adding slits to cylindrical and triangular pin fins enhanced thermal performance by promoting fluid mixing and recirculation. Similarly, Alam et al. [18] showed that increasing the level of inlet turbulence can boost heat transfer in triangular micro-pin-fins due to enhanced mixing and swirl generation.

Even though pin fins greatly enhance heat transfer, they do so at the expense of flow resistance. To mitigate this impact, grooves or dimples are often added, which boosts the heat transfer capability of a surface with a minor penalty in pressure drop. However, substituting the fins entirely with grooves or dimples may not yield sufficient thermal performance. Combining pin fins and dimples, forming a pin fin-dimple array, can then improve heat transfer without significantly increasing pressure drop [10,19].

Rao et al. [10] revealed that adding dimples to pin-fin arrays enhanced thermal performance due to increased turbulent mixing intensity near the walls. Moreover, this enhancement further increased with greater dimple depths, reaching a 15% increase in the overall performance compared with pins alone. In a similar study, Bi et al. [4] found that increasing depth improved the dimples' overall performance. However, both excessively large and excessively small dimple diameters reduced performance, and intermediate diameters were recommended. Further, Xie et al. [20] demonstrated that dimples can outperform both pins or protrusions, with teardrop dimples providing about 5% better performance than teardrop protrusions under similar conditions.

2.2 Influence of Attack Angle on the Heat Transfer Rate

Various approaches have been employed to improve the overall performance of fin arrays, including the introduction of tip-clearance [21–23], altering the inclination angle of pins in the streamwise direction [24–27], modifying the spanwise inclination angle (i.e. angle of attack) [28–30], and incorporating twist angles into the pins [31–33]. However, not all modifications guarantee enhanced heat transfer rates. For example, introducing tip-clearance or altering the streamline inclination angle can sometimes reduce both heat transfer and pressure loss within a channel, depending on the angle or clearance introduced [24–26,34]. To address this challenge, adjusting the attack angle can possibly result in an increased heat transfer while reducing pressure loss.

Several studies have explored the relationship between the attack angle (α) and thermo-hydraulic performance of pin fins, consistently indicating that performance of the pins is highly sensitive to α. Abdelmohimen et al. [35] observed that altering α in inline-arranged winged-pins deteriorated thermal performance, while α of 22.5° in staggered arrangements improves Nu by up to 45%, depending on Reynolds number (Re), and simultaneously reduces the friction factor (f) by 16%. Ali et al. [15] found that rotating square pin fins by 45° increases Nu by up to 68%, and further enhancement to 108% was achieved when α was reduced to 22.5°.

Ho et al. [36] experimentally demonstrated that airfoil-shaped fins achieved *Nu* enhancement of 19.9% at α = 0° compared with circular pins. This improvement increased to 22.5% and 25.2% as α rose to 10° and 15°, respectively, and is attributed to vortex formation along the airfoil. Acharya [37] found that the thermal performance of square pin fins at α = 0° and α = 45° was comparable, although the pressure loss was slightly higher for the α = 45° case under similar flow conditions.

Pallikonda et al. [38] identified that the optimal *Nu* for elliptical pins occurs at α = 6°, with a heat transfer enhancement of 122%-174% relative to α = 0°, depending on *Re*. Pressure loss, however, increased with α, reaching 57%-120% higher at α = 12° compared with α = 0°. Lee et al. [39] reported that oblique fins achieved up to 50% higher *Nu* at α = 27° than at α = 45°, while pressure loss increased by about 26% in the α = 27° case. *Nu* further improved by 21% at α = 15° compared α = 27°, but with a 47% higher pressure loss penalty.

Sallar et al. [40] showed that the highest thermal performance for I-shaped pins was achieved at α = 45° and 75°, where *Nu* increased by approximately 27%. This, however, was at the expense of pressure loss, which increased by 107% at α = 45°. Kangude et al. [41] observed that the thermal resistance of oblique-cut fins decreased by 8%-19% at a 60° oblique angle and by 22%-29% at 40°. However, this thermal performance improvement was accompanied by increased pressure loss, which reached up to 44% and 15% higher for 40° and 60° oblique angles, respectively.

The effect of feature angle relative to the flow direction on selected pin fins from the literature is summarized in Fig. 4. It is clear that the thermal performance of pin fins can be significantly affected and often improved by rotating them relative to the flow direction. However, in most configurations, this improvement comes at the cost of increased pressure drop. Some configurations achieve a moderate enhancement in thermal performance with a slight reduction in pressure loss [4], while others yield substantial thermal improvements but incur a significant pressure penalty [22]. This observation suggests that the performance of pin fins can be readily modified by adjusting α in a way that can be tailored to meet specific application requirements. Additionally, the pressure drop penalty can be mitigated by modifying the structure of the arrays, with a common approach being to incorporate of grooves or dimples into the pins.

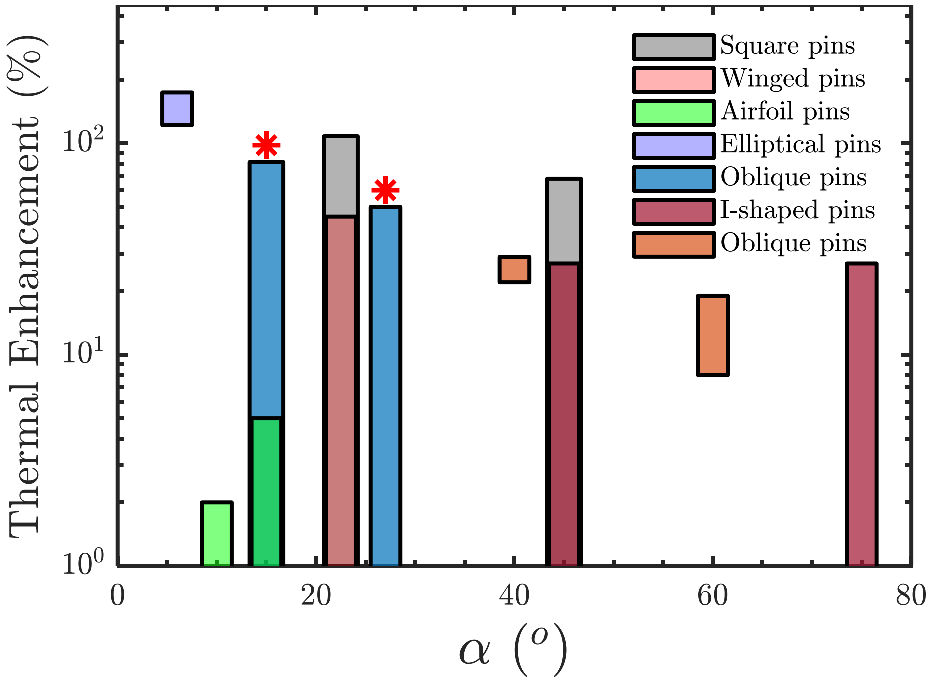

Fig. 4. Thermal enhancement in different pin types as a function of α. Each bar showcases an increase in *Re* as thermal enhancement increases. Enhancement is referenced to a baseline case of α = 0°, except for the pins marked with (*), where the reference is 45°. The pin arrays include square pins [6], winged pins [4], airfoil-shaped pins [20], elliptical pins [22], oblique pins* [23], I-shaped pins [24], and oblique pins [25].

2.3 Research Objectives

The reviewed literature clearly demonstrates that the performance of pin fins can be readily modified by adjusting their size, shape, spacings, density, and orientation in a way that can be tailored to meet specific application requirements. In this regard, the current study investigates the thermal-hydraulic performance of hook-shaped fins and dimple arrays under various sizes, flowrates, tip-clearances, and attack angles.

Khaled et al. [14] conducted the first single-phase experimental characterization of GRIPMetal thermal and hydraulic performance for rectangular channels. The results show that the hooks and grooves led to an enhancement in Nu compared with a flat surface by factors ranging between 3 and 4.6, depending on the tip clearance and Re. Additionally, f decreased by increasing tip clearance. The results from this work were limited to the turbulent regime and focused primarily on a single GRIPMetal feature size. Additionally, these tests were conducted with the arrays of hooked features placed on opposite sides of a rectangular channel, which may result in fluid interactions between the surfaces, and therefore not be representative for many instances of convection enhancement on a single surface.

The objective of this study is to build upon the work of Khaled et al. [14] to systematically quantify the thermal and hydraulic performance of three different sizes and array geometries of GRIPMetal surfaces in both laminar and turbulent regimes. Experiments were conducted at Reynolds numbers ranging between 600 and 12000, and the channel height was adjusted to capture the influence of tip clearance on the array performance. Furthermore, regression correlations were developed to establish relationships for Nu and f in terms of the geometry and fluid flow. These correlations will serve as design tools to optimize the design of heat exchangers using GRIPMetal surfaces for specific applications. Additionally, the thermal-fluidic performance of GRIPMetal arrays was evaluated across a range of α, from 0° to 90°, in increments of 22.5°. The assessment was conducted at *Re* ranging from 600 to 5000, with the arrays fully shrouded inside the channel. To gain deeper insights, the study also examines the associated temperature and flow structures, providing a comprehensive understanding of the arrays' performance.

Chapter 3

Experimental Setup

3.1 GRIPMetal Array Geometry

GRIPMetal arrays are created by partially removing metal from a surface, forming a hooked shaped raised fin, and leaving behind a groove that has approximately the same volume as the hook, as illustrated in Fig. 5. This study tested three different GRIPMetal arrays (mini, standard, and heavy) which varied primarily in hook length, inter-hook spacing, and dimple spacings. These arrays were created by adjusting the tooling and manufacturing parameters.

Each unit cell consists of two groups of hooks and their corresponding grooves (see Fig. 6a). Each group is oriented to one side of the streamwise direction, with a clearance separating the groups, and comprises two hook–dimple sets that are arranged in a staggered configuration. An array is formed by repeating the unit cell in both the streamwise and spanwise directions.

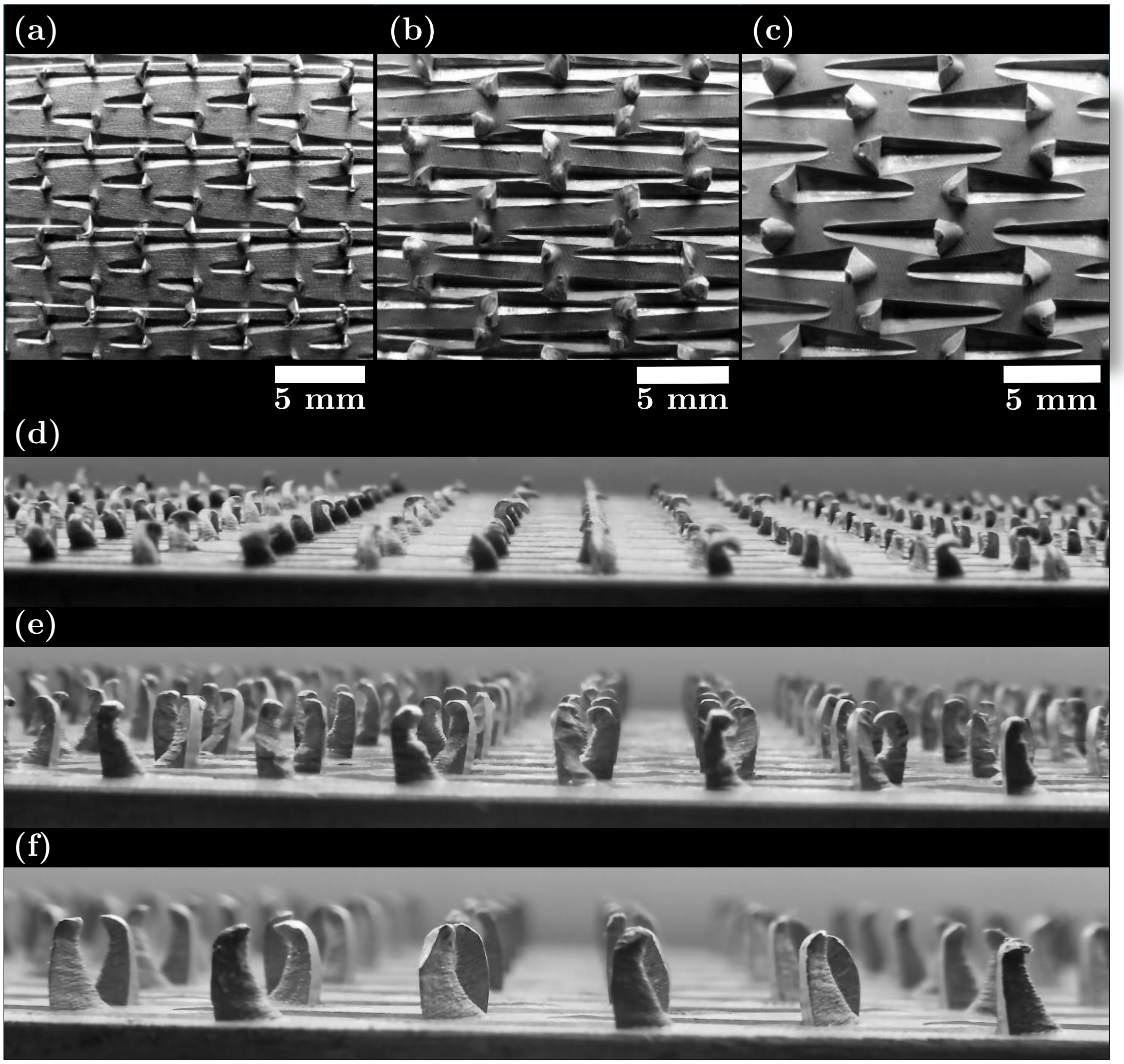

Fig. 5. Microscopic images showing plan and side views of the GRIPMetal arrays. Plan view: (a) mini, (b) standard, and (c) heavy arrays. Side view: (d) mini, (e) standard, and (f) heavy arrays.

The array geometry is described by streamwise spacing between the hooks within each group (S_L), spanwise spacing between each group set (S_T), and spanwise spacing between the hooks within each group (C_h), hook width (W_h), hook length (L_h), groove length (L_g), and hook height (h), as shown in Fig. 2b. The numerical values for these geometrical features are summarized in Table 1, represented by their mean values and standard deviations (S.D.).

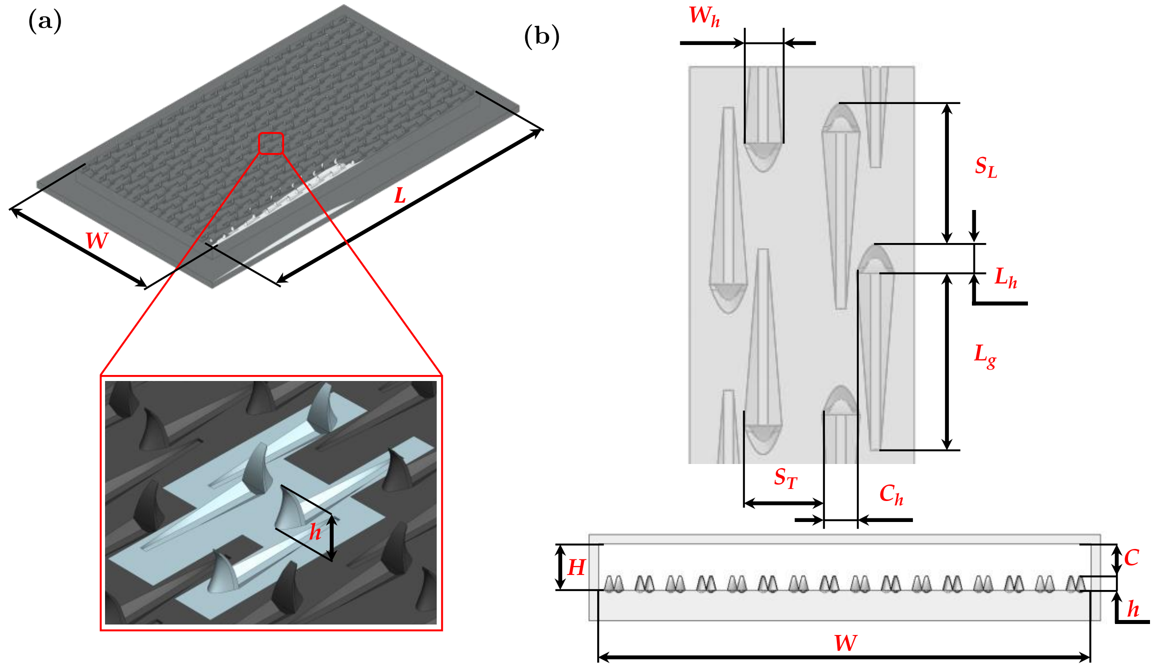

Fig. 6. *Schematic of the GRIPMetal arrays: Array with (a) a magnified unit cell and (b) geometrical parameters of the array with its orientation in the test channel.*

Table 1. Geometrical parameters of the GRIPMetal arrays.

Array Type	h	S_L	S_T	C_h	W_h	L_h	L_g
	Mean ±S.D. (mm)						
Mini	1.0 ±0.1	2.7 ±0.1	1.2 ±0.1	1.1 ±0.1	0.8 ±0.1	0.6 ±0.1	3.2 ±1.3
Standard	1.5 ±0.2	3.2 ±0.2	1.8 ±0.1	0.8 ±0.1	1.1 ±0.1	1.0 ±0.1	5.5 ±0.3
Heavy	2.3 ±0.1	4.5 ±0.2	2.8 ±0.1	1.5 ±0.1	2.0 ±0.1	1.4 ±0.1	6.1 ±0.3

3.2 Test Section and Experimental Setup

The experimental flow loop used to characterize the convective heat transfer and pressure drop of the GRIPMetal surfaces is shown in Fig. 7. Water was circulated through the loop by a stainless-steel rotary vane pump (Fluid-O-Tech PA1011) coupled to a 1 hp 90 VDC motor. The flow rate was controlled using a variable speed DC motor controller (IRONHORSE GSD5). Two flowmeters, installed in parallel, were used to measure a wide range of flow rates: The high-range flowmeter measured 1–30 LPM (OMEGA FTB604B) and the low-range flowmeter measured 0.1–2.5 LPM (Vision BV1000-025). During testing, flow was directed through the required flowmeter using on–off valves. A 5 μm filter was installed before the flowmeters, according to the flowmeter installation recommendations, to remove debris flowing to the test section. A pressurized accumulator tank was placed between the pump and the filter to dampen high-frequency pressure pulsations from the pump. Water leaving the test section was passed through a heat exchanger where it was cooled to 17°C via a BOYD RC–045 chiller.

The test section is shown in Fig. 8. Water entered the test section via the inlet plenum and flowed over the heated surfaces. Heat was applied by a copper heater block fastened to the bottom of the arrays. Temperatures were recorded at four locations within the arrays to thermally characterize performance. The test section is primarily constructed from aluminum (Al 6061) and consists of a top and bottom housing separated from each other by a spacing shim, with inlet and exit plenums attached to the top housing. Several shims with different thicknesses were used to adjust the hydraulic diameter. The arrays were inserted in a PEEK spacer, which was fastened to the middle of the bottom housing and acted as a heat break between the tested surfaces and the housing. The arrays had a transparent polycarbonate cover, which was fastened to the top housing. The transparent cover contained two ports upstream and downstream of the test section to enable differential pressure measurement. The tested array plates were 50.8 mm × 100 mm × 11 mm (Al6061). One was a bare, smooth plate, and the other had GRIPMetal hooks. The copper heater block was heated by four 200 W Dalton Electric cartridge heaters (3.1 mm diameter, 50.8 mm length) powered by an 840 W dual output DC power supply (Aim–TTi CPX400DP). A thin layer of thermal paste was applied at the interface between the heater block and the test plates to minimize contact resistance. The heater block sat on calcium silicate insulation that was attached to a bottom support plate.

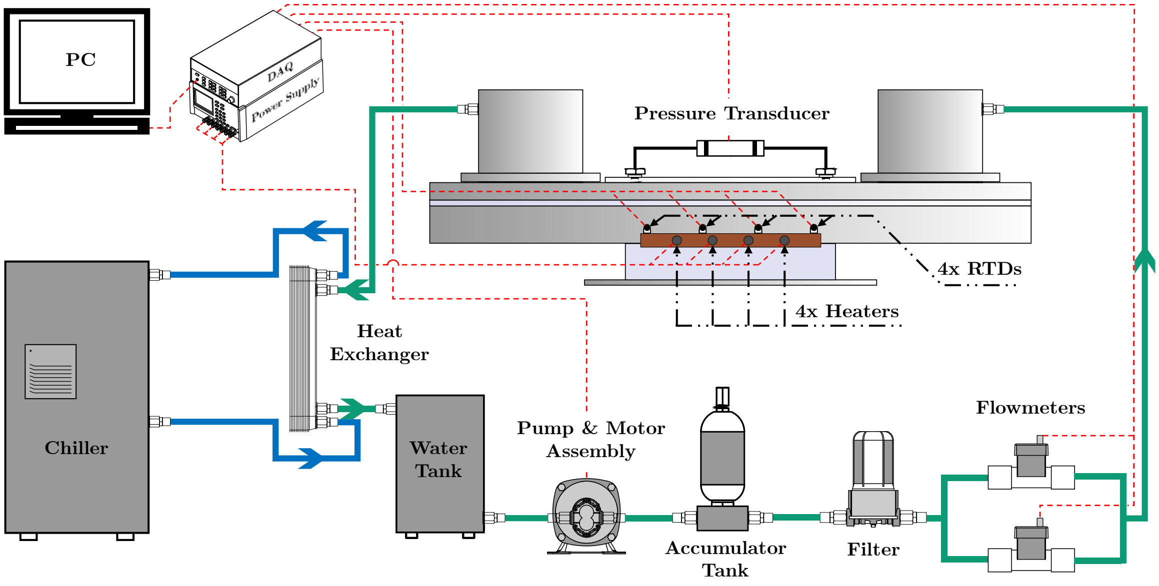

Fig. 7. Schematic diagram of the test section and experimental setup.

Four 3mm-diameter sheathed PT100 RTDs (4-wire configuration) were used to measure the temperatures of the test plates (Fig. 8), and they were placed at a distance δ of 8 mm below the plate surface (see Fig. 9). Two additional RTDs measured test section water inlet and outlet temperatures, and another monitored the ambient temperature. The seven RTDs were all calibrated to within 0.02 K of each other. The pressure drop across the test section was measured using one of two differential pressure transducers (DPTs; OMEGA PX409-030DWUV and OMEGA PX409-001DWUV) depending on the magnitude of the pressure drop. Experiments were performed on the arrays at several channel heights, resulting in different tip clearances (*C*) above the hooks, as shown in Fig. 6b. The power supplied to the heaters was adjusted depending on the flow rate to minimize uncertainty in the HTC, resulting in heat fluxes that ranged from 3 to 16 W/cm^2 (see section 3.7).

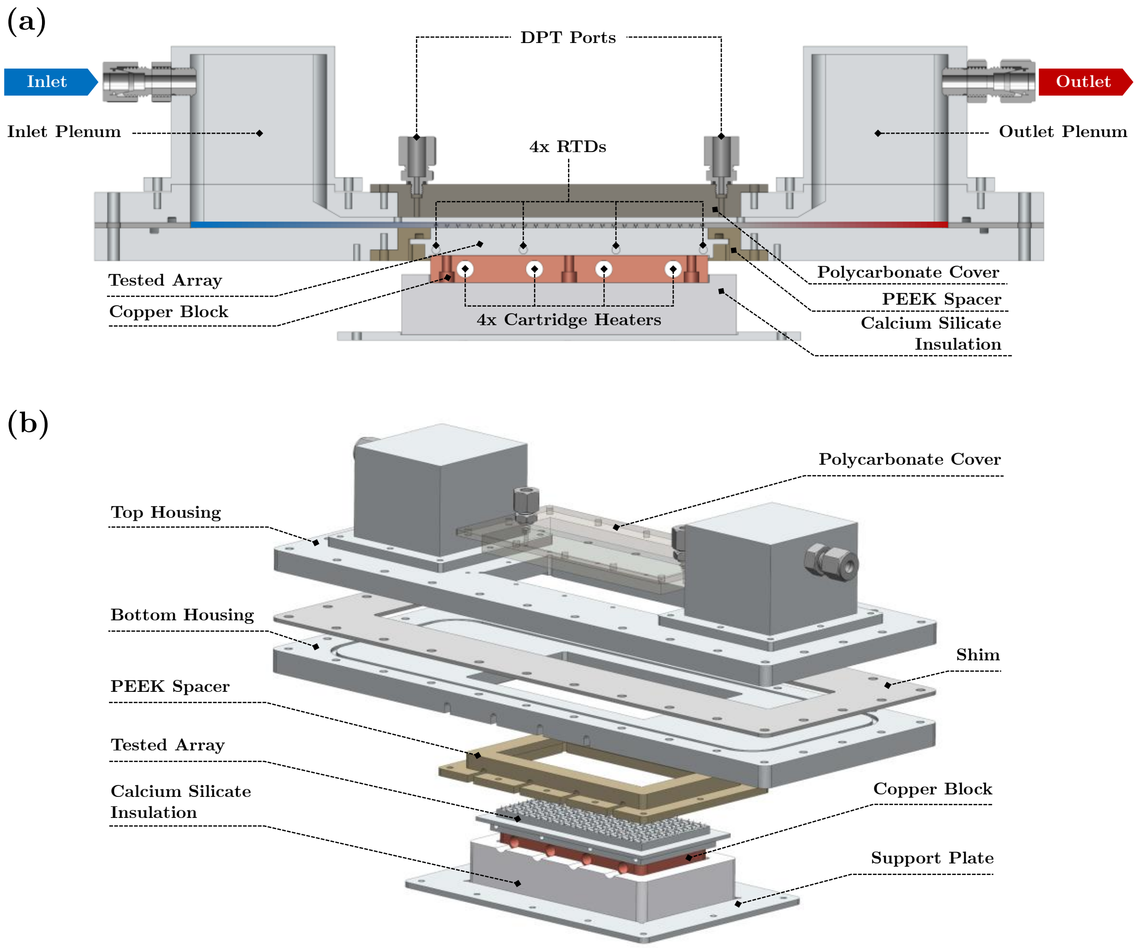

Fig. 8. Views of the test section: (a) cross-sectional view and (b) exploded view.

3.3 Data Reduction

A cross-sectional view of the test section channel showing key measurement locations is shown in Fig. 9. The surface temperature of the channel, $T_{s,x}$, was extrapolated from the RTD readings using the 1-D Fourier conduction equation,

$$T_{s,x} = T_{RTD,x} - \frac{Q_{in,net}}{A_o}\left[\frac{\delta}{k_{Al}}\right] \tag{3.1}$$

where $T_{s,x}$ is the array surface temperature at location x; $T_{RTD,x}$ is the reading of the RTD at location x; δ is the distance between the center of the RTDs and the array surface; k_{Al} = 167 W/mK is the thermal conductivity of the Al6061 array; A_o is the base surface area of the array; and $Q_{in,net}$ is the net input power from the heaters, which can be expressed as

$$Q_{in,net} = E \times I - Q_{loss} \tag{3.2}$$

where Q_{loss} is the heat lost to the surroundings, E is the supplied voltage, and I is the current flowing through the heater wires. The surface area of the array is expressed as

$$A_o = L \times W \tag{3.3}$$

where L and W are the length and width of the channel, respectively, as indicated in Fig. 6*a*.

The characteristic length-based averaged Nusselt number Nu_{L_c} was used to characterize the thermal performance of the tested arrays, expressed as

$$Nu_{L_c} = \frac{h_{avg} L_c}{k} \tag{3.4}$$

where h_{avg} is the average HTC over the surface; k is the thermal conductivity of water; and L_c is the characteristic length of the arrays, which is either equal to the hook height h or the channel hydraulic diameter, D_h, expressed as

$$D_h = \frac{2WH}{W + H} \tag{3.5}$$

The water thermal conductivity was evaluated at its mean bulk temperature, T_{bulk}, given by

$$T_{bulk} = \frac{T_{in} + T_{out}}{2} \tag{3.6}$$

where T_{in} and T_{out} are the inlet and outlet water temperatures through the rectangular channel, respectively. The average heat transfer coefficient, h_{avg}, was calculated as

$$h_{avg} = \frac{Q_{water}}{A_o \Delta T_{avg}} \tag{3.7}$$

where ΔT_{avg} is the average temperature difference between the heated surface and the bulk water temperature, expressed as

$$\Delta T_{avg} = \frac{1}{4} \sum_{x=1}^{4} (T_{s,x} - T_{w,x}) \tag{3.8}$$

where $T_{w,x}$ is the water bulk temperature at location x along the streamwise direction. This was calculated by measuring the water temperature at the entrance of the test section, where the flow is isothermal, and assuming a linear temperature rise along the test section.

The hydraulic performance of the arrays was quantified using the hydraulic diameter-based friction factor inside the channel, f_{D_h}, which can be expressed as

$$f = \frac{\Delta P}{\left(\frac{L}{D_h}\right)\rho_w V_{avg}^2/2} \tag{3.9}$$

where ΔP is the pressure loss across the test section, and V_{avg} is the area-averaged flow velocity inside the channel, expressed as

$$V_{avg} = \frac{Q_{flow}}{WH} \tag{3.10}$$

where Q_{flow} is the volumetric flow rate inside the channel measured by the flowmeters. The Reynolds number based on the channel hydraulic diameter Re was calculated as

$$Re = \frac{\rho_w V_{avg} D_h}{\mu_w} \tag{3.11}$$

where μ_w is the absolute viscosity of water evaluated at T_{bulk}.

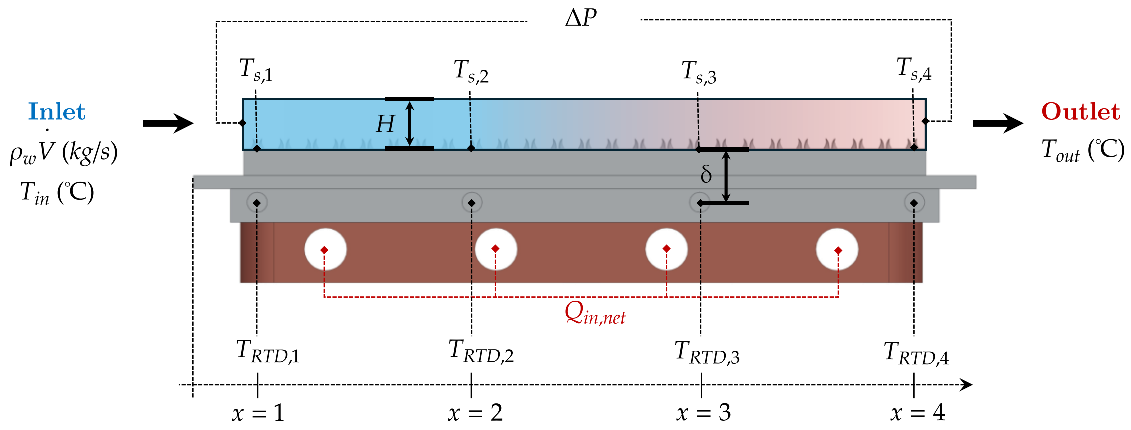

Fig. 9. Data reduction of the GRIPMetal arrays depicting water flow over the hooks inside the test channel.

3.4 Heat Loss Calibration and Energy Balance

Heat loss from the test section to the surroundings was quantified by supplying heat at a relatively low power to the heater block under dry (no flow) conditions. For a given input power, the temperature of the heater block and test plate was increased until steady-state and the heat supplied by the heaters equaled the heat loss to the surroundings, Q_{loss}. The input power (which is being dissipated as heat lost to the surroundings) was then correlated to the temperature difference between the average plate temperature and the ambient temperature using linear regression which resulted in an empirical estimate for heat loss as

$$Q_{loss} = 0.1 \sum_{x=1}^{4} T_{RTD,x} - 0.4\, T_{amb} \tag{3.12}$$

where T_{amb} is the ambient temperature. The maximum heat lost to the surroundings accounted for only 2% of the total heat supplied by the heaters.

An energy balance of the net heat supplied by the electric heaters and that gained by the flowing water can be expressed as

$$Q_{water} = Q_{in,net} + Q_{viscous} = \rho_w Q_{flow} C_{p,w} (T_{out} - T_{in}) \tag{3.13}$$

where Q_{water} is the heat gained by water; ρ_w is the density of water; $C_{p,w}$ is the specific heat capacity of water; T_{in} and T_{out} are the inlet and outlet water temperatures from the rectangular channel, respectively; and $Q_{viscous}$ is the viscous heating due to pressure drop across the test section, expressed as

$$Q_{viscous} = \Delta P \times Q_{flow} \tag{3.14}$$

Both ρ_w and $C_{p,w}$ were evaluated at T_{bulk}.

3.5 Overall Thermal-Hydraulic Performance

The enhancement in heat transfer achieved by adding fins is typically accompanied by a significant increase in pressure drop [5]. To address this, a comparison was conducted utilizing the thermal enhancement factor (η_o) proposed by Webb and Eckert [42], calculated at equal pumping power, and formulated as

$$\eta_o = \frac{St/St_o^*}{(f/f_o^*)^{\frac{1}{3}}} \tag{3.15}$$

where St and St_o^* are the Stanton numbers for the finned and smooth surfaces, respectively, while f and f_o^* are the friction factors for the finned and smooth surfaces. Eq. (3.15) is frequently misused when evaluating the performance of a certain finned or roughened surface [43]. Many studies mistakenly evaluate St, St_o^*, f, and f_o^* at the same Re, while others substitute Stanton number with Nusselt number [4,6,8,10,14]. Using the same Re for finned and unfinned surfaces while keeping the geometry fixed violates the constant pumping power constraint. For this regard, both St_o^* and f_o^* are evaluated at an equivalent Reynolds number, Re_o^*, which is expressed as

$$Re_o^* = \left(\frac{f}{f_o^*}\right)^{\frac{1}{3}} Re \tag{3.16}$$

where Re is the Reynolds number for the finned surface. The evaluation of St_o^* and f_o^* at Re_o^* ensures that the constant pumping power constraint is fulfilled while maintaining a fixed channel geometry [43].

An equivalent expression of Eq. (3.15) can be achieved by substituting the definition of the Stanton number, $St = Nu\ (Re\ PR)^{-1}$, into Eq. (3.15) while utilizing Eq. (3.16) which yields

$$\eta_o = \frac{Nu}{Nu_o^*} \tag{3.17}$$

where *Pr* is the Prandtl number and Nu^*_o is the Nusselt number for a smooth surface. Eq. (3.17) is equivalent to Eq. (3.15), and it represents the correct form of η_o to be utilized at constant pumping power when using the Nusselt number as long as the surface geometry is fixed.

3.6 Baseline Testing Using a Smooth Surface

The Shah and London [44] correlations were used to describe the laminar *Nu* and *f* for the flat plate.

$$Nu_o = 2.236\left(\frac{L}{D_h\, Re\, Pr}\right)^{1/3} + 0.9 \tag{3.18}$$

$$f_o = \frac{96}{Re}\left(1 - \frac{1.3553}{a} + \frac{1.9467}{a^2} - \frac{1.7012}{a^3} + \frac{0.9564}{a^4} - \frac{0.2537}{a^5}\right) \tag{3.19}$$

where *L* is the length of the test section and $a = W/H$ is the aspect ratio of the channel. For the turbulent flow regime, the Nusselt [45] and Blasius [46] correlations (Eqs. (3.20) and (3.21)) were used to calculate Nu_o and f_o, respectively.

$$Nu_o = 0.036\, Re^{0.8}\, Pr^{1/3}\left(\frac{D_h}{L}\right)^{0.055} \tag{3.20}$$

$$f_o = \frac{0.3164}{Re^{*0.25}} \tag{3.21}$$

where Re^* is the modified *Re* that establishes a geometric similarity between circular ducts and rectangular channels, which was calculated as per [47]:

$$Re^* = \phi^*(a)\, Re \tag{3.22}$$

$$\phi^*(a) \cong \frac{2}{3} + \frac{11}{24\, a}\left(2 - \frac{1}{a}\right) \tag{3.23}$$

3.7 Uncertainty Analysis

The RTDs were calibrated in a temperature-controlled bath of Julabo F32–HE between 10–70˚C in 5˚C steps. The calibration process yielded a maximum deviation of ±0.02˚C in the uncertainty of the RTDs. Uncertainties of the measured parameters for the other sensors are summarized in Table 2.

Uncertainties of the calculated parameters were estimated using the propagation of error method proposed by Kline and McClintock [48]. Assuming F is a function of N variables x_k, the uncertainty in F (ω_F) is estimated from the uncertainty in x_k (ω_{x_k}) as

$$\omega_F = \left[\sum_{k=1}^{k=N}\left(\frac{\partial F}{\partial x_k}\omega_{x_k}\right)^2\right]^{1/2} \tag{3.24}$$

Using the method of error propagation described in Eq. (3.24), the maximum uncertainties in the calculated *Re*, f_{D_h}, and *St* were less than 8%, 13%, and 22%, respectively, with the high uncertainty for *St* occurring only at large channel heights and low *Re*.

A sensitivity analysis was performed to minimize the uncertainty in h_{avg}. For this purpose, the flat plate was used as a benchmark, and the inlet water temperature was kept constant at 23˚C. The heat flux to the plate was varied to change the outlet water temperature, and the uncertainty in h_{avg} was calculated for each input heat flux at several *Re* (1,000–15,000, increments 1,000) while keeping the remaining parameters constant.

The Shah and London correlation [44] (Eq.(3.18)) and the modified Dittus-Boelter correlation [49] (Eq. (3.25)) were used to evaluate *Nu* over the flat plate for the cases where $Re < 3{,}000$ and $Re > 3{,}000$, respectively.

$$Nu = 0.023\, Re^{0.8}\, Pr^{0.4} \varphi \tag{3.25}$$

where φ is a correction factor that accounts for the thermally developing flow, and it depends on the magnitude of L relative to the developing layer length (L_d), which is expressed as in Eq.(3.26). Values of φ for $L/L_d < 1$ and $L/L_d > 1$ are shown in Eqs. (3.27) and (3.28), respectively.

$$L_D = 0.693\, Re^{0.25}\, D_h \tag{3.26}$$

$$\varphi = \left[1.11 \left(\frac{Re^{0.2}}{(L/D_h)^{0.8}}\right)\right]^{0.275} \tag{3.27}$$

$$\varphi = 1 + \frac{0.144\, Re^{0.25}}{L/D_h} \tag{3.28}$$

Table 2. Uncertainties of the measured quantities.

Measured Parameter	Uncertainty
Temperature difference	±0.02˚C
Pressure drop	±0.08% from full scale reading (±0.08% FS)
Flow rate	3% of reading for Vision BV1000-025 and 1% of reading for OMEGA FTB604B
Voltage	±0.1% of reading
Current	±0.3% of reading
Length	±0.05 mm

Chapter 4

Experimental Results and Discussion

4.1 Sensitivity Analysis

The variation of the relative uncertainty in h_{avg} with the increase in the water temperature is shown in Fig. 10. Fig. 10 reveals that the relative uncertainty in h_{avg}, denoted by ω_F / h_{avg}, initially exhibits a high value, reaching up to 9%, at low differences between the mean temperature of the channel surface and the bulk fluid. However, as the heater power increases and the temperature difference between the surface and the fluid increases, this uncertainty drops significantly and stabilizes at an asymptotic value after 1–2°C temperature difference, depending on *Re*.

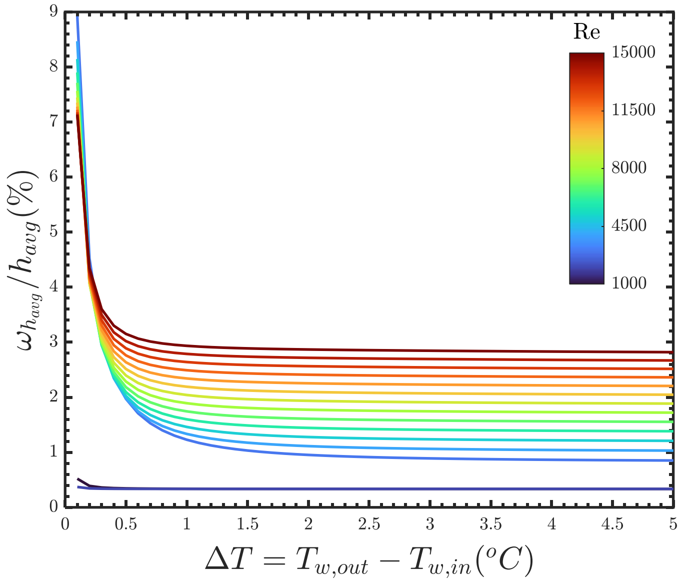

Fig. 10. The variation of the relative uncertainty in havg (ω_F/ h_{avg}) with the increase in the input power to the test section at several Re. Calculations were performed for a flat plate with channel height H = 1 mm.

4.2 Energy Balance and Baseline Testing

A summary of the energy balance between the measured input power and the power from the water temperature rise for all arrays and channel heights is shown in Fig. 11. In all cases, the energy balance is within the experimental uncertainties and within ±10%. For 99% of the test data, it is within ±5%. This agreement validates the test setup and the heat loss calibration procedure.

Plate temperature measurements confirmed uniformity across the plate, where the deviation between the highest plate temperature and the average RTD readings was consistently below 0.4˚C. Repeatability of the experimental results was established through repeated tests following test section disassembly and reassembly, with consistent Nusselt number and friction factor results within the calculated uncertainty limits.

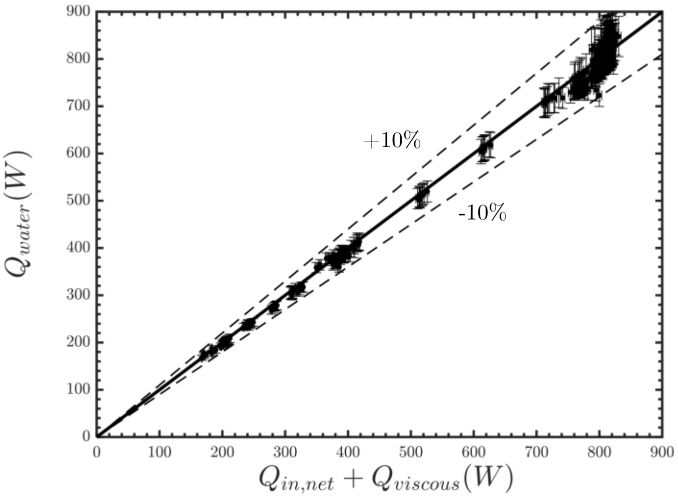

Fig. 11. Energy balance between the net heat supplied by the heaters and viscous heating with the energy gained by water.

To validate the test setup and establish a baseline for thermal-hydraulic performance, a smooth plate was characterized in terms of Nu_o and f_o which were compared with predictions from previously established correlations. A comparison of the error between the experimental Nu_o and f_o obtained in the current study for the smooth channel with respective correlation predictions is presented in Fig. 12*(a)* and *(b)*. These plots illustrate the percentage errors between the experimental Nusselt number ($Nu_{o,exp}$) and friction factor ($f_{o,exp}$) and those predicted by the correlations, denoted as ε_{Nu_o} and ε_{f_o}, respectively. ε_{Nu_o} and ε_{f_o} are expressed as

$$\varepsilon_{Nu_o} = \frac{Nu_{o,exp} - Nu_{o,corr}}{Nu_{o,exp}} \tag{4.1}$$

$$\varepsilon_{f_o} = \frac{f_{o,exp} - f_{o,corr}}{f_{o,exp}} \tag{4.2}$$

The average errors between $Nu_{o,exp}$ and the predictions from the correlations were 6.7% and 5.3% for the laminar and turbulent regimes, respectively. Considering the uncertainty, approximately 94% of the experimental $Nu_{o,exp}$ values aligned with the correlation prediction within ±10%. For $f_{o,exp}$, the average errors were 9% and 8.4% for the laminar and turbulent regimes, respectively. Approximately 87% and 100% of the experimental $f_{o,exp}$ data agree with the correlations within ±10% and ±15%, respectively.

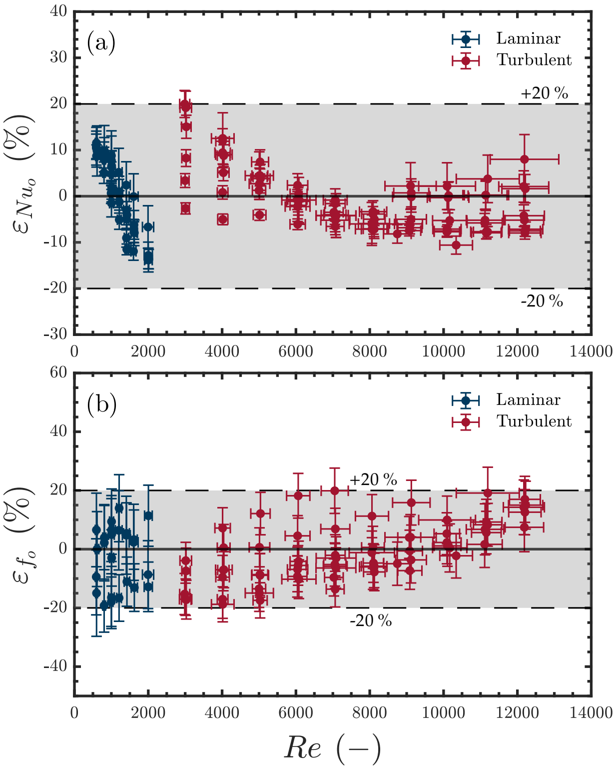

Fig. 12. Comparison of the error between the experimental (a) Nu_o and (b) f_o obtained in the present work with their corresponding correlation-predicted values.

The slight differences between the experimental Nu_o and f_o and the correlation predictions can be attributed to several factors such as the channel high aspect ratio, wall roughness, and thermally developing flow. Fig. 12 reveals that the highest deviation occurs at *Re* between 1,000 and 5,000, which can be attributed to the flow being transitional in that regime. Bi et al. [4] reported similar deviation at *Re* < 5,000, attributing it to higher turbulence in finned channels compared to smooth channels at the same *Re*, which makes the flow close to fully turbulent at those *Re*, thereby making the results for the finned channels more accurate than smooth ones. Nevertheless, the agreement within the uncertainty limits between the experimental data and the correlation prediction ensures the validity of the heat loss calibration procedure, data reduction approach, and the overall experimental setup, which is a preliminary step for testing the arrays and ensuring reliable results.

4.3 Thermal Performance of GRIPMetal Arrays

The thermal performance of the GRIPMetal arrays is presented in the form of Nu_{D_h}. The enhancement in heat transfer for the mini, standard, and heavy hooks relative to that of the smooth channel (Nu_{D_h}/Nu_o) was evaluated at several channel heights, corresponding to several clearance-to-height ratios, and the results are summarized in Fig. 13. The introduction of hooks and dimples into the tested plates led to a significant improvement in heat transfer compared with that of smooth plates (i.e., the enhancement ratio was greater than 1 across the entire *Re* range tested).

For all arrays, the enhancement ratio increased with *Re* until it reached a peak in the transitional regime (around $Re \approx 3{,}000$), after which the enhancement gradually declined, reaching an asymptotic value as *Re* increased further. For the same channel height, the heavy arrays exhibited the highest thermal performance enhancement, followed closely by the standard arrays, while the mini arrays consistently showed the lowest enhancement. This is because of the decrease in tip clearances between cases: As the tip clearance decreases, the generation of severe turbulences and separated shear layers intensifies due to the sharp tips of the hooks becoming closer to the end wall. These phenomena contribute to enhanced fluid mixing, leading to increased heat transfer rates.

The heavy arrays demonstrated enhancement ratios ranging between 3.7 and 5.7 relative to the flat plate, with the maximum enhancement ratio occurring at $Re = 3{,}000$ and the highest Nu_{D_h} was 477.6, both observed at the minimum channel height of $H = 2.268$ mm. For the standard arrays, the highest performance was observed at $H = 2.02$ mm, achieving an Nu_{D_h} of 498.46, and the enhancement relative to the smooth channel ranged between 3.4 and 5.7. The maximum relative enhancement occurred at $Re = 3{,}000$ and the same channel height.

In contrast, the mini arrays exhibited lower performance compared with the heavy and standard arrays, with enhancement ranging between 2.4 and 4.5 relative to the smooth channel. The highest enhancement ratio occurred at $Re = 3{,}000$ and $H = 1.00$ mm, while the highest Nu_{D_h} attained in this case was 336.9 at $H = 4.115$ mm.

While the highest thermal performance occurred at the smallest channel height for the heavy arrays, this was not the case for the standard and mini surfaces, where the highest Nu_{D_h} occurred at a larger hydraulic diameter. This discrepancy is due to the decrease in the hydraulic diameter as the channel height decreases, leading to an increase in the HTC. However, this decrement in hydraulic diameter outweighed the increase in the HTC when transitioning from the second smallest channel height to the smallest one for both the standard and mini arrays, resulting in a slight decrease in Nu_{D_h}. Instead of hydraulic diameter, the Nusselt number can be defined based on the hook height (Nu_h), which represents the dimensionless HTC without considering changes in the channel hydraulic diameters. Using this new description of Nusselt number, the highest Nu_h for the standard and mini arrays were 392.4 and 277.6, occurring at H = 1.64 mm and H = 1.00 mm, respectively.

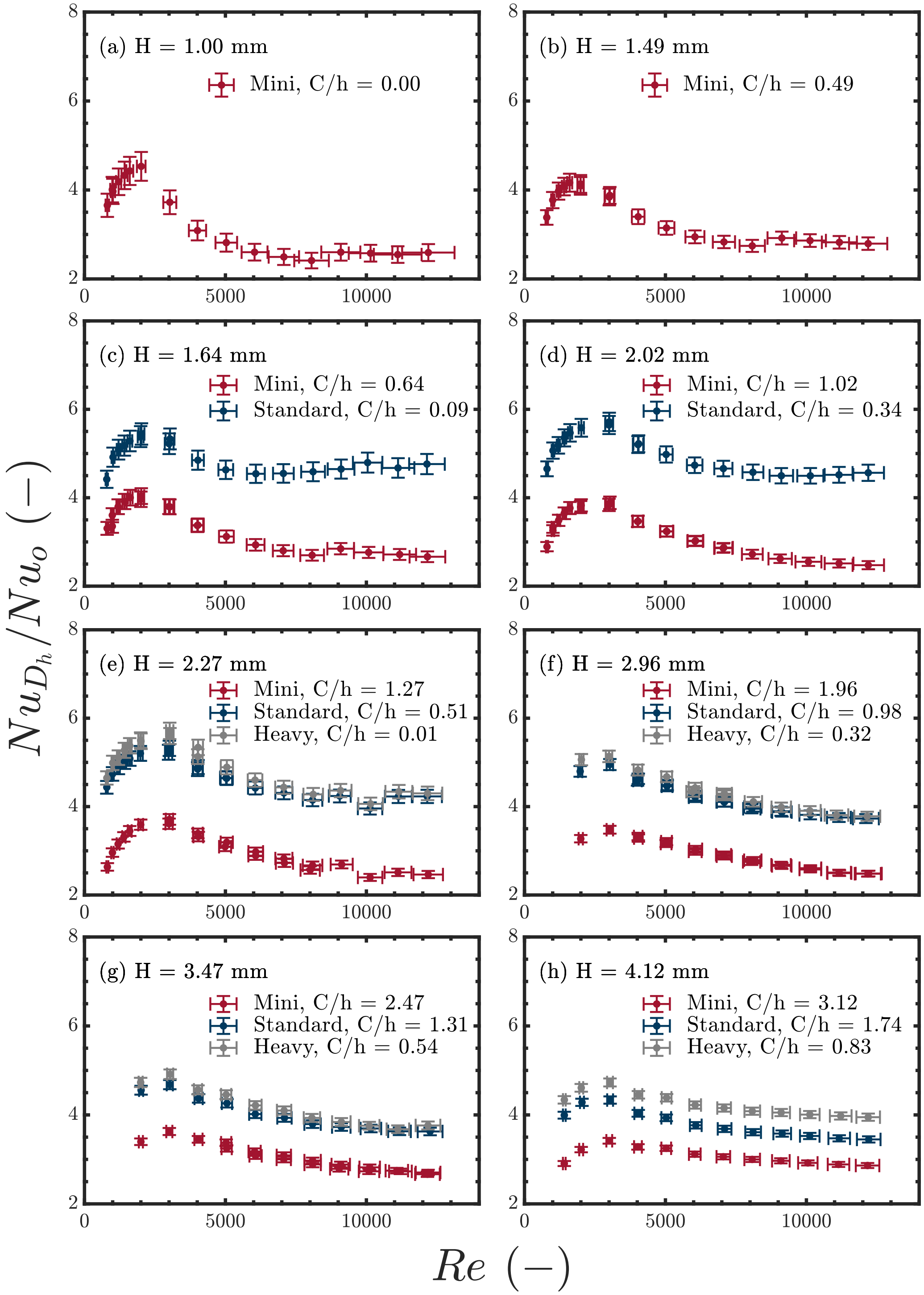

Fig. 13. Thermal enhancement ratio for the mini, standard, and heavy arrays relative to the flat plate (Nu_{D_h}/Nu_o) obtained at several channel heights (H): (a) $H = 1.00$ mm, (b) $H = 1.49$ mm, (c) $H = 1.64$ mm, (d) $H = 2.02$ mm, (e) $H = 2.27$ mm, (f) $H = 2.96$ mm, (g) $H = 3.47$ mm, and (h) $H = 4.12$ mm.

4.4 Effect of Tip Clearance on the Thermal Performance of GRIPMetal Arrays

The impact of tip clearance on the thermal performance of the arrays is shown in Fig. 14. Here, the thermal performance of each array at a specific tip clearance and *Re*, expressed by Nu_h, is compared with that of the hook at the minimum tip clearance ($Nu_{h,C}$) at the same *Re*, which were 0% and 0.8% for the mini and heavy arrays, respectively, and 8.5% for the standard ones. From Fig. 14, it is evident that the thermal performance of the hooks diminishes as the tip clearance increases. This is because a decrease in tip clearance results in a more compact flow path and a higher restriction to the flow in the channel, thereby enhancing the thermal performance of the arrays, a phenomenon that has been observed in previous studies for pin fins [1,50,51]. Additionally, at the same tip clearance, the enhancement was slightly more pronounced at lower *Re*, a trend that was more noticeable for the standard and heavy arrays compared with the mini hooks.

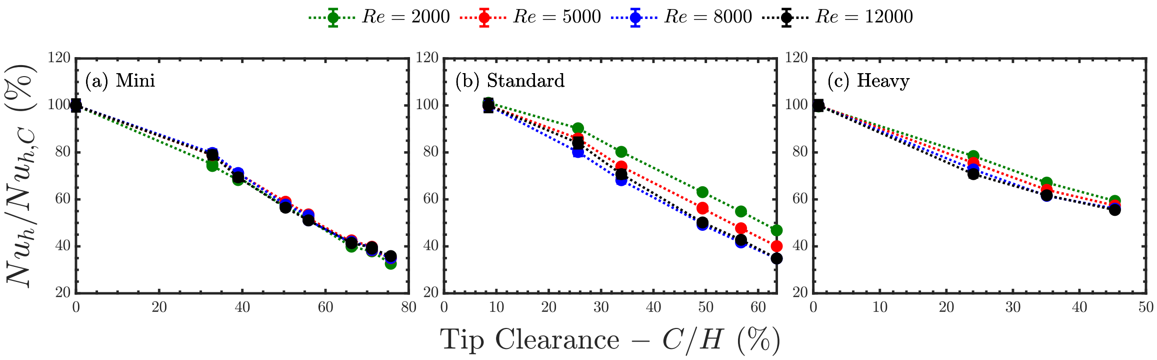

Fig. 14. Effect of tip clearance on the thermal performance of the (a) mini, (b) standard, and (c) heavy arrays.

Interestingly, the variation in $Nu_h/Nu_{h,C}$ at a specific tip was relatively insensitive to *Re*. The mini arrays exhibited the least scatter in $Nu_h/Nu_{h,C}$ at the same tip clearance across different *Re*, with the scatter being limited to 5%. On the other hand, the scatter increased for the heavy and standard arrays, reaching 7% and 14%, respectively. This higher scatter for the standard arrays is attributed to the slightly elevated reference tip clearance (8.5%) compared with the mini and heavy arrays.

Moores and Joshi [52] showed that the introduction of clearances initially enhances the thermal performance of the fins because of the additional tip area exposed to the flow. A further increase in tip clearance, however, degrades the performance as the effect of the fluid bypassing the arrays becomes more dominant. Similar findings were reported by Chyu et al. [53]. In the present study, the tip area of the hooks is too small to cause a noticeable increase in the thermal performance of the arrays at small tip clearances, which makes the fluid bypassing effect more obvious. In agreement with the present findings, Mousa [1] showed that the thermal performance of the fins will continue to degrade with an increase in *Re* as the tip clearance increases beyond zero, which provides the highest restriction to the flow.

A comparison of the thermal enhancement at the same tip clearance is shown in Fig. 15*(a–c)* where three different tip clearances were used: 34 ±1%, 50 ±5%, and 56 ±1%. Fig. 15 shows that the mini arrays consistently have the lowest thermal enhancement ratio compared with the heavy and standard arrays at the same tip clearance. The thermal enhancement of the mini arrays was 22%–54% lower than that of the standard arrays and 14%–58% lower than that of the heavy ones, depending on the tip clearance and *Re*.

The standard arrays exhibited slightly higher thermal performance than the heavy arrays, with an increase of 1%–15% across all *Re* ranges, except at high *Re* with at 50 ±5% tip clearance. The higher performance of the standard arrays can be attributed to a narrower spanwise gap between the hooks than on the heavy arrays; the spanwise spacing minus hook width (S_T - W_h) for the standard arrays is about 12% lower than for the heavy arrays. Additionally, standard arrays have the smallest C_h among all GRIPMetal arrays, which is 47% and 28% lower than heavy and mini arrays, respectively. This smaller spacing can result in higher resistance to the flow and thus enhance thermal performance. Additionally, Elkholy et al. [13] found that the standard arrays provided slightly greater surface area to the flow compared with the heavy arrays.

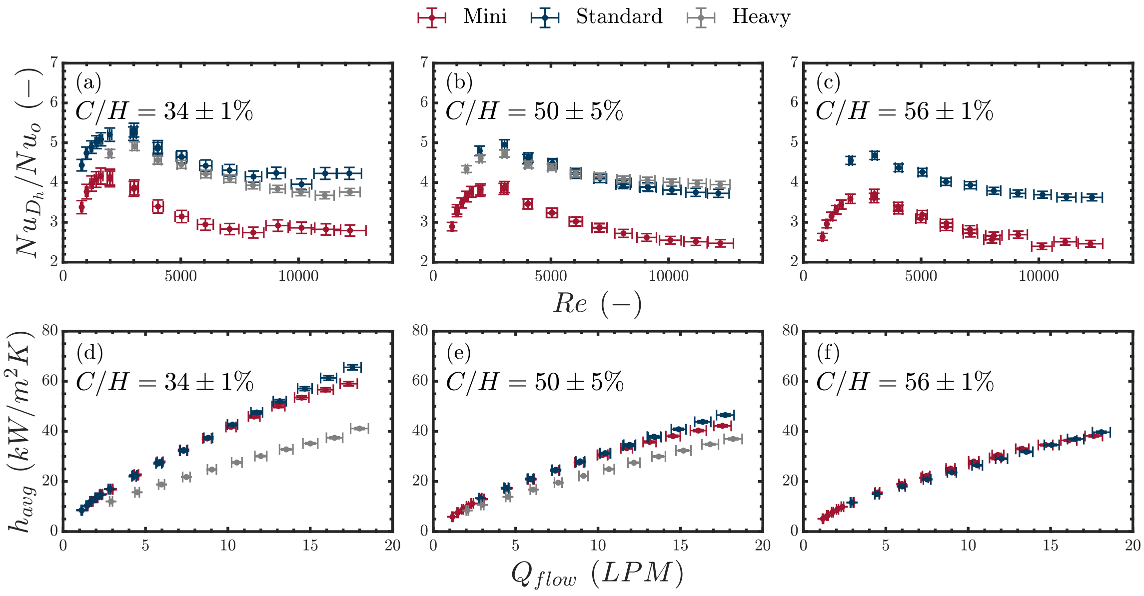

Fig. 15. Comparison of the thermal enhancement between mini, standard, and heavy arrays at the same tip clearance: thermal enhancement ratio (Nu_{D_h}/Nu_o) at (a) 34 ±1%; (b) 50 ±5%; and (c) 56 ±1% tip clearance, and HTC (havg) at (d) 34 ±1%; (e) 50 ±5%; and (f) 56 ±1% tip clearance.

The thermal enhancement of the arrays relative to an unfinned surface, expressed as the ratio Nu_{D_h}/Nu_o, can be misleading, especially when considering the geometrical features of the arrays. For instance, in the same study, Elkholy et al. [13] reported that among the three GRIPMetal arrays, the mini hooks had the highest surface area and therefore would be expected to exhibit the highest thermal performance. To further explore this, the heat transfer coefficient was plotted against the flow rate, as shown in Fig. 15*(d–f)*. The Reynolds number in Eq. (3.11) is expressed in terms of the flow rate and the channel dimensions:

$$Re = \frac{2\rho_w Q_{flow}}{\mu_w W\left(1 + \frac{H}{W}\right)} \tag{4.3}$$

In this study, due to the high aspect ratio of the channel which ranges from 12 to 51, Eq. (4.3) can be approximated as

$$Re = \frac{2\rho_w Q_{flow}}{\mu_w W} \tag{4.4}$$

During testing, the channel width was kept constant. Assuming the thermal properties of water remain relatively constant, *Re* can be considered directly proportional to the volumetric flow rate inside the channel, i.e., $Re \propto Q_{flow}$. Therefore, at the same tip clearance, a plot of h_{avg} versus flowrate expresses the heat transfer coefficient for the arrays at nearly the same *Re* (see Fig. 15*(d − f)*). This relationship can explain the thermal behavior of the arrays depicted in Fig. 15*(a–c)*, regardless of the smooth surface behavior or any geometrical differences.

The standard and mini arrays have similar heat transfer coefficients at any flow rate, although the standard arrays show slightly higher values at high flow rates. In contrast, the heavy arrays have the lowest h_{avg}. The mini arrays feature the lowest streamwise and spanwise spacing between the hooks and the largest surface area, as outlined by Elkholy et al. [13]. Conversely, the standard arrays feature overlapping hooks within the same group ($C_h < W_h$) and the highest groove-to-hook-length ratio—about 25% and 4% higher than that of the heavy and mini arrays, respectively. Bi et al. [4] numerically demonstrated that dimples create secondary flows within their cavities, which can enhance heat transfer between the fluid inside their cavities and the mainstream. Both factors—small spacings and longer grooves—favor the mini and standard arrays, resulting in both arrays having a similar heat transfer coefficient.

Heavy arrays have the widest spacings between the hooks, with streamwise spacing 67% larger than for mini arrays and spanwise spacing 56% and 134% wider than for standard and mini arrays, respectively. Additionally, heavy arrays have the smallest surface area exposed to the flow. These factors contribute to the heavy arrays having the lowest heat transfer coefficient. However, as the tip clearance increases, the HTC of the heavy arrays becomes comparable to that of the mini and standard arrays. This suggests that the arrays function as a surface roughness at larger tip clearances.

4.5 Fractional Contribution of Fluid Mixing to Thermal Performance

The thermal performance parameters Nu and h_{avg}, account for both improved fluid mixing/induced turbulence and the increased specific surface area created by the fins. Since the specific surface areas of the GRIPMetal arrays differ and only the projected area (A_o) is used in the calculation of h_{avg} (see Eq.(3.7)), the resulting Nu and h_{avg} inherently include the area factor. To isolate the impact of flow mixing or increased turbulence from surface area effects, Nu_{D_h}/Nu_o is divided by the area factor. According to Elkholy et al. [13], the area factors are 1.8, 1.56, and 1.35 for the mini, standard, and heavy arrays, respectively. A comparison of the thermal enhancement due to fluid mixing among the mini, standard, and heavy arrays at the same tip clearance is given in Fig. 16.

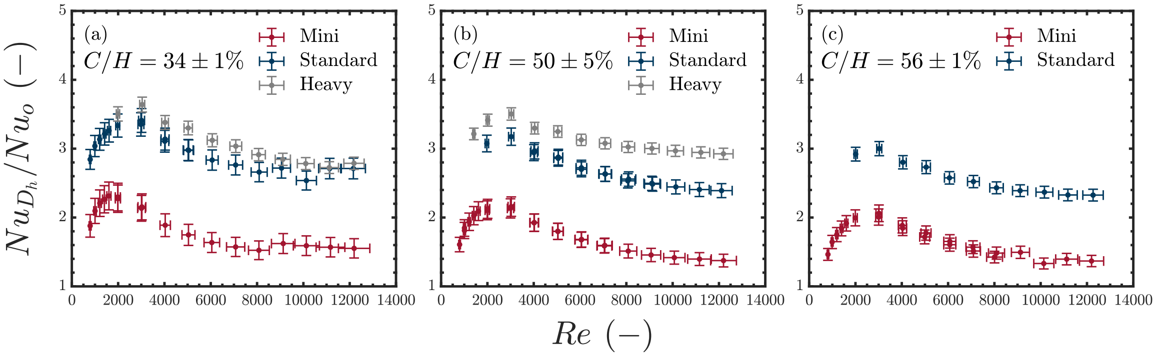

Fig. 16. Comparison of the thermal enhancement due to fluid mixing between mini, standard, and heavy arrays at the same tip clearance: thermal enhancement ratio (Nu_{D_h}/Nu_o) at (a) 34 ±1%; (b) 50 ±5%; and (c) 56 ±1% tip clearance.

Mini arrays showed the lowest thermal enhancement ratio similar to Fig. 15(a-c), which was 41%-78% and 53%-113% lower than standard and heavy arrays, respectively, depending on the tip clearance and *Re*. Heavy and standard arrays exhibit similar performance at small tip clearance across all *Re* values, with heavy arrays outperforming slightly at 50 ±5% tip clearance. On average, the thermal performance of the heavy arrays was 1%-23% higher than that of the standard arrays.

Overall, the GRIPMetal arrays significantly outperform unfinned surfaces, with 56%, 65%, and 74% of the thermal enhancement attributed to fluid mixing for the mini, standard, and heavy arrays, respectively (as can be calculated by taking the inverse of the area factor). The remainder of the enhancement comes from the increased specific surface area of the features.

4.6 Hydraulic Performance of GRIPMetal Arrays

Although the addition of hooks to the surfaces improved heat transfer capabilities, this enhancement came at the cost of increased pressure drop through the channel. The variation of the ratio of the array friction factor, f_{D_h}, to that of the smooth channel, f_o, at different *Re* is shown in Fig. 17, denoted by f_{D_h}/f_o. The friction factor ratio increased sharply at lower *Re*, with the increase becoming less pronounced and nearly constant thereafter.

The primary factor affecting f_{D_h}/f_o was found to be the array type: For a given channel height, mini arrays exhibited the lowest friction factor, followed by the standard ones, while the heavy arrays showed the highest f_{D_h}/f_o. This can be attributed to the increased fraction of water flowing through the spaces between the hooks because of the smaller clearance between hook tips and the channel top wall.

For the heavy arrays, the highest pressure drop was observed at the smallest channel height, $H = 2.27$ mm, with f_{D_h}/f_o of 15.56 ±1.85. The highest friction factor ratios for the standard and mini arrays were 12.00 ±1.46 and 7.05 ±1.10 and occurred at $H = 2$ mm and $H = 1$ mm, respectively.

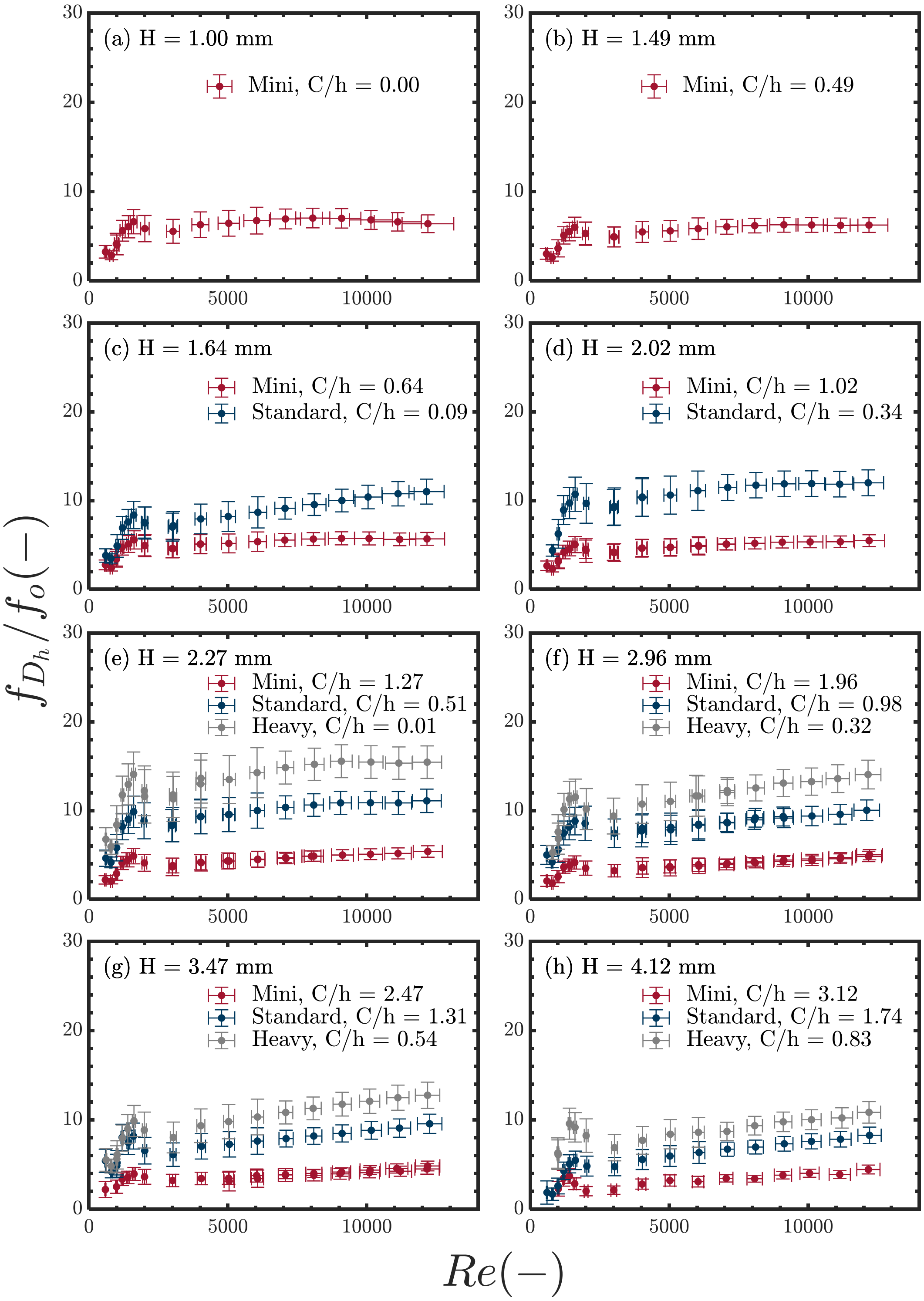

Fig. 17. Comparison of the friction factor ratios for the mini, standard, and heavy arrays to those for the flat plate (f_{D_h}/f_o) obtained at several channel heights (*H*): (a) *H* = 1.00 mm, (b) *H* = 1.49 mm, (c) *H* = 1.64 mm, (d) *H* = 2.02 mm, (e) *H* = 2.27 mm, (f) *H* = 2.96 mm, (g) *H* = 3.47 mm, and (h) *H* = 4.12 mm.

4.7 Effect of Tip Clearance on the Hydraulic Performance of GRIPMetal Arrays

A comparison of array hydraulic performance at the same tip clearance is shown in Fig. 18(a–c). Among all tested arrays, mini arrays offered the least flow resistance ratio relative to a smooth channel. The hydraulic performance of the mini arrays was 52%–148% better than that of the standard arrays and 54%–108% better than that of the heavy arrays, depending on the tip clearance and *Re*. The standard and heavy arrays exhibited similar hydraulic performance across the tested *Re* ranges. Although the heavy arrays showed a marginally higher f_{D_h}/f_o at large *Re*, this difference was within the measurement uncertainty.

The hydraulic performance of the arrays is better understood by examining the pressure drop across them, like the havg used in describing the thermal performance in Fig. 15(a–c). Despite having the best hydraulic performance relative to a smooth surface, the mini arrays exhibited the highest pressure drop. This is due to two factors: First, the small inter-fin spacings between the hooks increase the form drag imposed by the arrays on the flow. Second, the high surface area of the mini arrays results in significant skin friction. These drag components cause the mini arrays to have the highest pressure drop compared with the other arrays at the same tip clearance.

The standard arrays exhibited a pressure drop lower than the mini arrays, which can be attributed to the larger inter-fin spacings and the slightly longer groove length compared with hook length. According to Bi et al. [4], unlike fins, dimples do not offer significant flow resistance to the mainstream flow, but they enhance circulation and secondary flows inside their cavities, improving the heat transfer between the fluid inside the cavity and the mainstream flow. This confirms the results in Fig. 15(d–f). In contrast, heavy arrays have the lowest pressure drop at the same tip clearance due to having the largest streamwise and spanwise spacings, as well as the smallest surface area. Similar to the behavior of the havg, the pressure drop across the arrays becomes more similar as the tip clearance increases. This is mainly because a larger fraction of the stream flows through the clearance, and the hooks behave more like surface roughness.

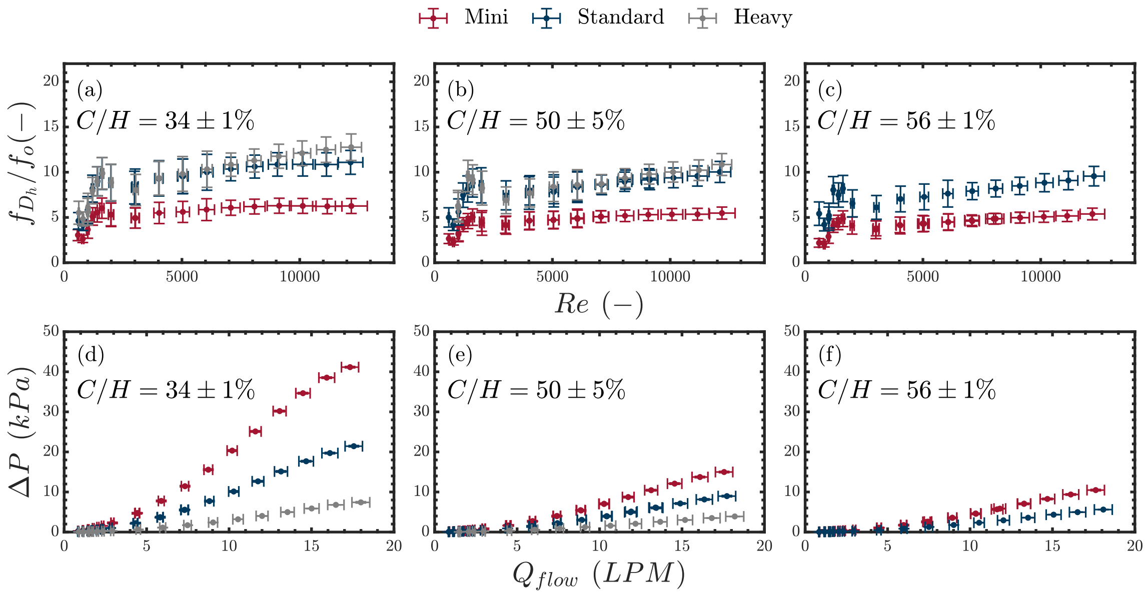

Fig. 18. Comparison of the hydraulic performance between the mini, standard, and heavy arrays at the same tip clearance: hydraulic performance ratio (f_{D_h}/f_o) at (a) 34 ±1%; (b) 50 ±5%; and (c) 56 ±1% tip clearance, and ΔP at (d) 34 ±1%; (e) 50 ±5%; and (f) 56 ±1% tip clearance.

4.8 Overall Performance of the GRIPMetal Arrays

Correlations for Nu_o and f_o were developed for the smooth channel data obtained in the present work. For Nu_o, the parameters of the Nusselt correlation (Eq. (3.20)) were correlated with the experimental data across the entire flow regime, resulting in a correlation represented as

$$Nu_o = 0.0244\, Re^{0.8573}\, Pr^{0.4} \left(\frac{D_h}{L}\right)^{0.1263} \tag{4.5}$$

Eq.(4.5) has a relative Root Mean Square Error (rRMSE) of 4.4% and an adjusted R-squared value (R^2) of 0.995. All attempts to express f_o for the entire flow regime using a single correlation did not result in errors lower than those obtained with the Shah and London and Blasius correlations (Eqs. (3.19) and (3.21)). Therefore, two separate correlations were developed to represent the laminar and turbulent flows, given in Eqs. (4.6) and (4.7), respectively.

$$f_o = \frac{147.5145}{Re_o^{0.9854}}\left(\frac{1}{a}\right)^{0.1496} \tag{4.6}$$

$$f_o = \frac{1.4932}{Re_o^{0.4038}}\left(\frac{D_h}{L}\right)^{0.0269} \tag{4.7}$$

Eq. (4.6) has a rRMSE of 7% and an $R^2 = 0.82$, while Eq. (4.7) has a rRMSE of 9.8% and an $R^2 = 0.94$. Using Re^*_o, one can then evaluate St^*_o and f^*_o using Eqs. (4.5)–(4.7) and then substitute them into Eq. (3.15) to evaluate η_o. Because Eq.(4.7) was developed up to Re of 12,000, if the calculated Re^*_o exceeds 12,000, the Shah and London or Blasius correlations can be used to avoid any erroneous equivalent Reynolds number for the smooth channels.

The variation of η_o with Re for the mini, standard, and heavy arrays at different channel heights is demonstrated in Fig. 19. All arrays showed an improvement in the overall performance of the test section, as indicated by η_o being above one. Initially, η_o was high, at around 2–4 at low Re; then, it decreased as Re increased. Notably, the decrease in η_o at high Re followed an asymptotic trend, indicating that the performance of the arrays will consistently surpass that of the smooth surface at all Re. Additionally, at the same Re and channel height, all array types exhibited nearly the same η_o, especially at larger channel heights, while the distinction became more pronounced at lower channel heights.

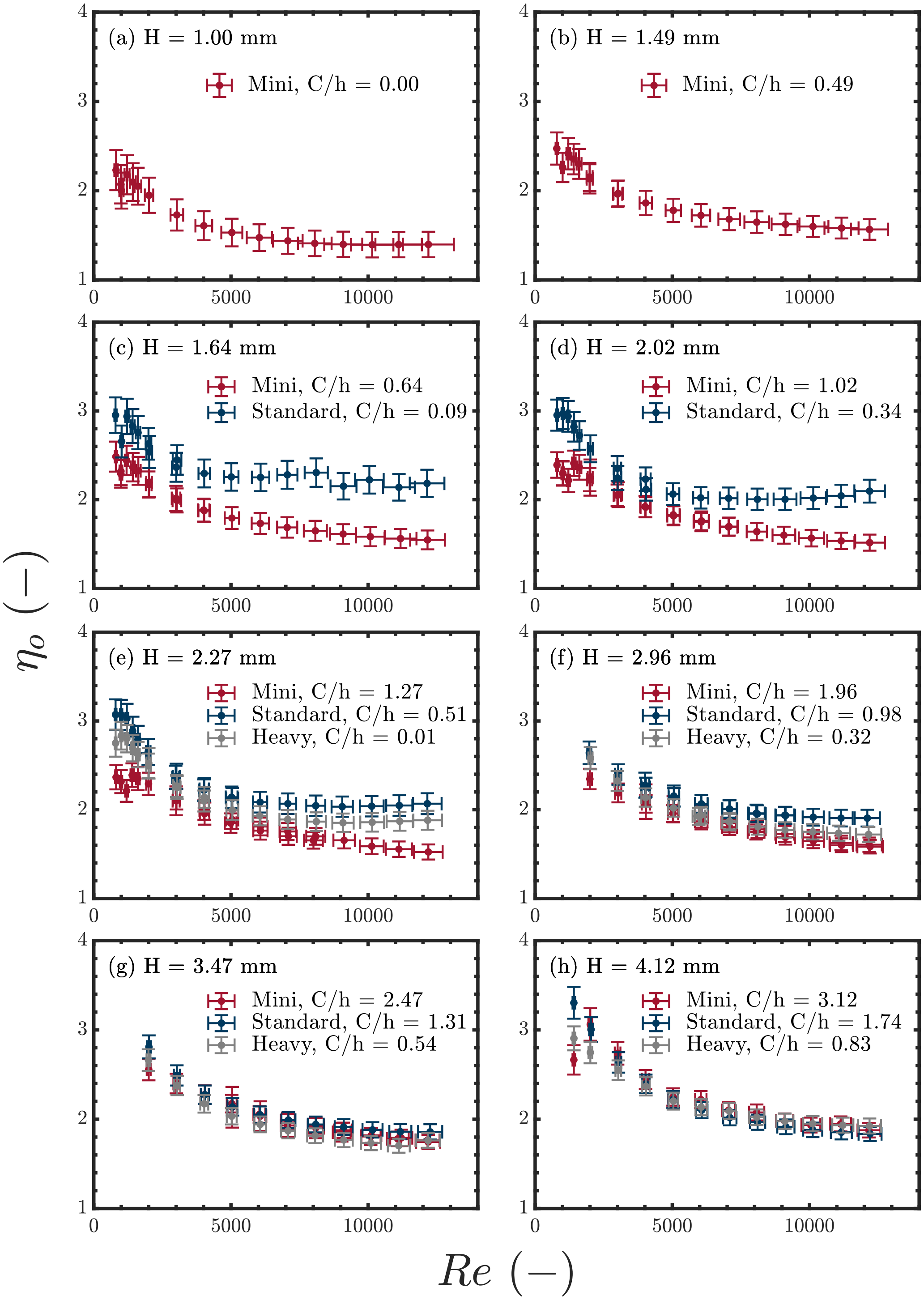

Fig. 19. The overall performance criterion (η_o) for the mini, standard, and heavy arrays at different channel heights (H): (a) $H = 1.00$ mm, (b) $H = 1.49$ mm, (c) $H = 1.64$ mm, (d) $H = 2.02$ mm, (e) $H = 2.27$ mm, (f) $H = 2.96$ mm, (g) $H = 3.47$ mm, and (h) $H = 4.12$ mm. (Note: The abscissa represents Re for the hooks, not to be confused with Re_o^* for the smooth channel.)

The standard arrays demonstrated the highest overall performance, with a maximum η_o of 3.30 ±0.18 at Re = 1,400 and H = 4.12 mm, and a minimum of 1.84 ±0.1 at Re = 12,000 and the same channel height. This indicates that the standard arrays offer optimized performance, in which it provides a trade-off between enhancing heat transfer while minimizing the pressure drop. The mini arrays followed with the second highest η_o, ranging between 3.06 ±0.18 at Re = 2,000 and H = 4.115 mm, and 1.39 ±0.14 at Re = 10,000 and H = 1 mm. The heavy arrays exhibited relatively lower performance, with η_o ranging between 2.91 ±0.13 at Re = 1,400 and H = 4.12 mm, and 1.70 ±0.08 at Re = 11,000 and H = 3.47 mm. Having η_o greater than unity signifies the effectiveness of the hook–dimple sets in enhancing heat transfer while incurring a small penalty in pressure drop. Results show that the maximum efficiency for all array types lies between 1,400 and 2,000, which is consistent with the findings of Alam et al. [18], who reported that the maximum performance was observed at Re between 1,000 and 3,000.

To investigate the impact of tip clearance, the overall performance of all three arrays is plotted against the clearance above the hooks as shown in Fig. 20. The overall thermal and hydraulic performance showed a more dispersed declining trend compared with the thermal performance alone. The standard and heavy arrays, unlike the mini ones, showed little sensitivity to tip clearance, where the scatter was limited to 15% and 10%, respectively.

Regardless of Re, the overall performance of the mini arrays increased almost exponentially relative to the zero-tip clearance case. For example, the highest performance for the mini arrays was observed at 76% tip clearance, with values of 157 ±18%, 147 ±16%, 146 ±16%, and 134 ±15% for Re = 2,000, Re = 8,000, Re = 5,000, and Re = 12,000, respectively. This increasing behavior of the overall thermal-hydraulic performance indicates that the effect of the reduction in pressure drop penalty across the arrays outweighed the deterioration in heat transfer as the tip clearance increases. This is different from the findings of Moores and Joshi [52], who reported that an optimal balance between improved heat transfer and minimized pressure drop penalty can be achieved by introducing small clearances—typically less than 10% of the fin height. This suggests that the optimum tip clearance depends on the application. If enhanced thermal performance is required without concern for pressure drop, a zero tip-clearance is ideal. However, if the objective is to improve thermal performance while minimizing pumping power, introducing tip clearance will be a better option.

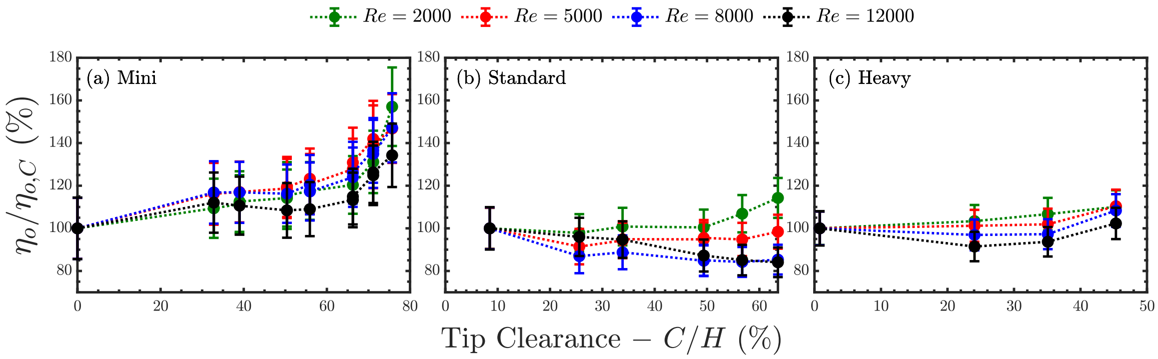

Fig. 20. Effect of tip clearance on the overall performance of the (a) mini, (b) standard, and (c) heavy arrays. The overall thermal-hydraulic performance (η_o) is expressed as a ratio to the performance at the minimum tip clearance for the array, $\eta_{o,C}$.

The overall performance of the arrays at the same tip clearance is illustrated in Fig. 21. Similar to the thermal performance shown in Fig. 16*(a–c)*, the standard arrays demonstrated the highest overall performance at the smallest tip clearance. The heavy arrays followed closely at low *Re*, but a slight deviation in performance emerged between the two arrays as *Re* increased. The difference in performance between the standard and heavy arrays was within 11% at 34 ±1% tip clearance, which diminished to 4% as the clearance increased to 50 ±5%. Mini arrays, on the other hand, exhibited the lowest overall performance, regardless of *Re* or tip clearance.

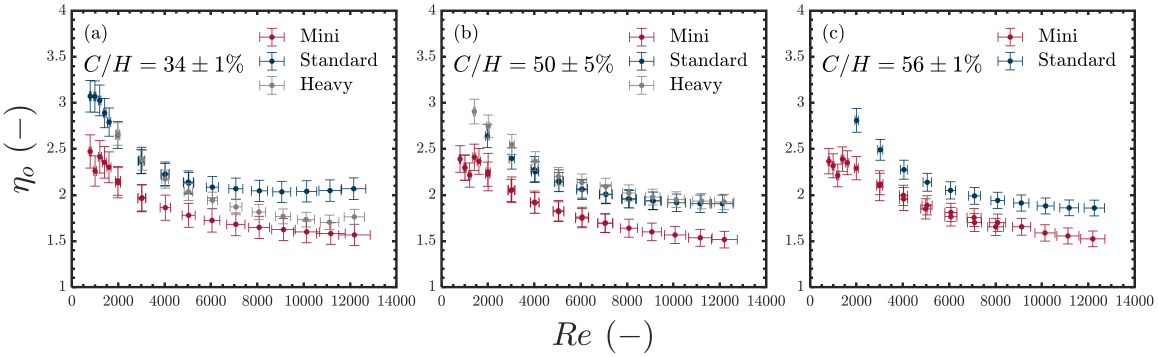

Fig. 21. Comparison of the overall thermal and hydraulic performance between the mini, standard, and heavy arrays at (a) 34 ±1%, (b) 50 ±5%, and (c) 56 ±1% tip clearance.

4.9 Nusselt Number and Friction Factor Correlations for GRIPMetal Arrays

The correlations for the Nusselt number and friction factor developed in Khaled et al.'s [14] study did not include any parameters to differentiate between the different hook geometries, and all hooks would exhibit the same values of Nusselt number and friction factor for the same *C*/*h*. While all array types had mostly the same Nusselt number, even though they were only tested on one *C*/*h*, this was not true for the friction factor, as all three types of arrays had considerable differences in f_h at the same *C*/*h*. For this reason, correlations should differentiate between the different array types.

All attempts to develop unified correlations for the Nusselt number and the friction factor incorporating the various geometrical aspects of the hooks resulted in correlations with significant errors. The shape of the hooks was observed to notably affect both the Nusselt number and friction factor, and this influence varied depending on whether the flow was laminar or turbulent. In this respect, separate correlations were developed for the Nu_h and f_{D_h} of each hook type under laminar and turbulent flow conditions using a particle swarm optimization code implemented in MALTAB. The developed correlations can be expressed as

$$Nu_h = a\,Re^b \left(1 + \left(\frac{C}{h}\right)\right)^c Pr^{0.4} \tag{4.8}$$

$$f_{D_h} = \frac{A}{Re^B} \tag{4.9}$$

$$A = \; a\left(\frac{C}{h}\right) + c \tag{4.10}$$

$$B = b\left(\frac{C}{h}\right) + d \tag{4.11}$$

where h is the hook height; C is the clearance between the hook tip and the channel (H - h), and a–d are correlation constants whose values are given in Table 3.

The errors between the mean Nu_h and f_{D_h} and their corresponding correlation predictions were found to be within 15% and 20%, respectively, for all hook types. Accounting for the uncertainty, 99% of the experimental Nu_h for the mini hooks were within ±10% of the predictions, while 92% of the data points showed errors within ±10% for f_{D_h}. For the standard hooks, 99% of the data points had errors lying within ±10% for Nu_h and 96% had errors within ±10% for f_{D_h}. Similarly, for the heavy hooks, all data points had errors within ±10% for Nu_h and 99% were within ±10%.

Table 3. Constants for the Nu_h and f_{D_h} correlations in Eqs. (4.8) **-** Error! Reference source not found. **.**

Nu_h

	Laminar ($Re \leq$ 2,300)					Turbulent ($Re >$ 2,300)				
	a	*b*	*c*	rRMSE (%)	R^2	*a*	*b*	*c*	rRMSE (%)	R^2
Mini	0.05	0.8	-0.8	4	1	0.1	0.7	-0.8	4	1
Standard	0.1	0.7	-0.8	3	1	0.1	0.8	-1	3	1
Heavy	0.1	0.7	-0.9	2	1	0.1	0.7	-1	3	1

f_{D_h}

	Laminar ($Re \leq$ 2,300)						Turbulent ($Re >$ 2,300)					
	a	*b*	*c*	*d*	rRMSE (%)	R^2	*a*	*b*	*c*	*d*	rRMSE (%)	R^2
Mini	0.0	0.03	2	0.2	6	0.9	0.0	0.03	3	0.3	1	0.9
Standard	2	0.2	0.7	0.07	10	0.7	4	0.1	2	0.2	3	0.9
Heavy	0.0	0.07	3	0.2	6	0.9	0.0	0.07	5	0.2	2	1

4.10 Comparison of the Performance of GRIPMetal Arrays with the Literature

To evaluate the relative overall performance of the GRIPMetal arrays, their thermal and hydraulic performance is compared with that of surface enhancement techniques previously investigated in the literature (see Fig. 22). These studies used arrays with geometrical features similar in size to those in the present study. Several factors were considered, including fin height, inter-fin spacing, hydraulic diameter, and Reynolds number. The comparison was based on several similar parameters, including the hydraulic diameter of the test channel (D_h), feature diameter (f_d), transverse pitch (f_p), feature height (f_h), and height-to-diameter ratio (f_h / f_d). For GRIPMetal arrays, hook width was taken as f_d, the average spanwise spacing between the hooks was considered equivalent to f_p, and hook height was taken as f_h. Detailed geometric similarities between the GRIPMetal arrays and those from the literature are shown in Table 4.

Overall, Fig. 22 shows that the mini and standard arrays outperformed the hemispherical dimples investigated by Bi et al. [4], with their performance being, on average, 32% and 91% higher than that of the dimples, respectively. This demonstrates the enhancing effect of the hooks on the GRIPMetal dimples, where they improve thermal performance without significantly increasing the pressure drop. The teardrop protrusions and dimples studied by Xie et al. [20] exhibited better performance compared with the hemispherical ones but still fell short of the performance of the GRIPMetal arrays. The mini arrays were, on average, 13% and 18% higher in performance than the protrusions and dimples, respectively, while the standard arrays were 69% and 77% higher.

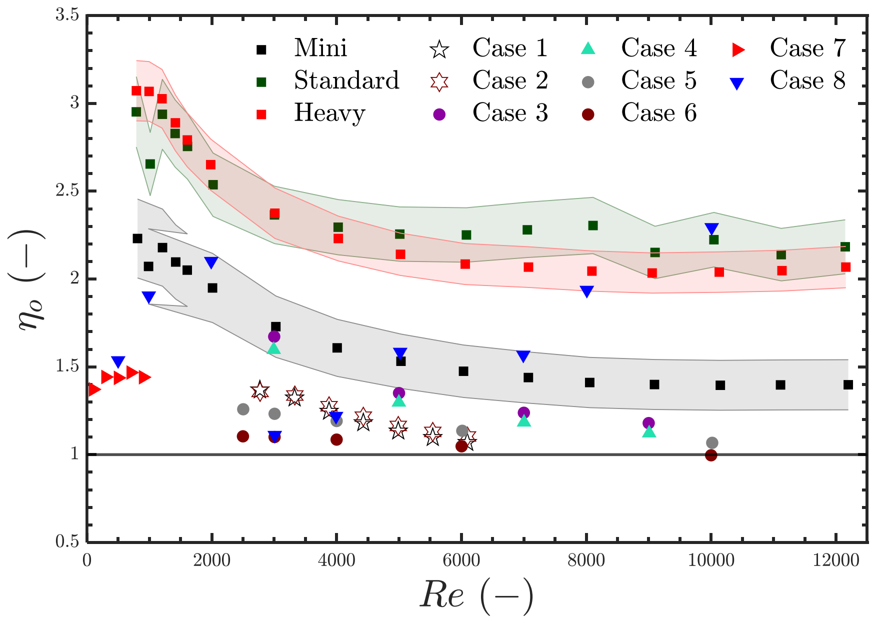

Fig. 22. Comparison between the overall performance of the GRIPMetal arrays with that of other surface enhancement techniques previously investigated in the literature. The highlighted regions indicate the uncertainty in performance of the GRIPMetal arrays.

Table 4. Geometric similarities between GRIPMetal arrays and other geometries from the literature.

Study	Case Number	Geometry	Equivalent GRIPMetal Array*	Parameter	Geometry Parameter Value	GRIPMetal Parameter Value
Bi et al. [4]	1	Hemispherical dimple	Mini	D_h	1.0 mm	2.0 mm
				f_d	0.96 mm	1.0 mm
			Standard	D_h	1.0 mm	3.2 mm
				f_d	0.96 mm	1.0 mm
Bi et al. [4]	2	Hemispherical dimple	Mini	D_h	1.0 mm	2.0 mm
				f_d	1.1 mm	1.2 mm
Xie et al. [20]	3	Teardrop dimple	Same as case 1			
	4	Teardrop protrusion				
Sun et al. [54]	5	Winglet delta pairs	Mini	f_h	0.60 mm	1.0 mm
	6	Winglet delta pairs with elliptical cylinder	Heavy	f_h	2.0 mm	2.2 mm
Zhou et al. [3]	7	Circular micropillar	Mini	f_h / f_d	1.2	1.0
Alam et al. [18]	8	Triangular pin fins	Heavy	f_h	2.5 mm	2.2 mm
				f_d	2.0 mm	1.6 mm
			Mini	f_h / f_d	1.2	1.0

* Performance of GRIPMetal arrays used in the comparison is based on zero or smallest tip clearance.

The winglet delta pairs with elliptical cylinder investigated by Sun et al. [54] showed relatively low performance compared with the heavy arrays, with its performance being about 91% lower. However, the winglet delta pairs alone performed slightly better, with its performance being 51% lower than that of the mini arrays.

The micropillars studied by Zhou et al. [3] had significantly lower performance compared with the mini arrays. The triangular pins of Alam et al. [18], on the other hand, exhibited a rapidly changing performance compared with the other geometries investigated. Initially, their performance was 9% lower than that of the mini arrays; then, it increased to become 7% higher at $Re \approx 2{,}000$. However, the performance dropped rapidly, reaching a turning point at $Re \approx 3{,}000$, after which it increased again, reaching a peak performance at $Re \approx 10{,}000$ that was 39% higher than the mini arrays. The heavy arrays, on the other hand, showed significantly better performance compared with the triangular pins at lower *Re*, though their performance degraded as *Re* increased.

Overall, the GRIPMetal arrays demonstrated significantly better performance compared with the geometries investigated, highlighting their enhanced thermal and hydraulic efficiency. Because of their relatively cheap and simple manufacturing process, the GRIPMetal arrays could present a promising alternative to conventional heat transfer enhancement techniques.

Chapter 5

Numerical Investigation

Experimental results demonstrate that GRIPMetal outperforms both smooth surfaces and conventional surface extensions reported in the literature. Beyond the introduction of tip clearance, another approach to modifying the performance of GRIPMetal arrays is adjusting their orientation relative to the flow direction. As discussed in section 2.2, previous studies have shown that tilting pin fins at an angle can significantly alter their thermal-hydraulic performance. Given GRIPMetal's robust and cost-effective manufacturing process, further improving its performance through strategic orientation would enhance its superiority over traditional surface extension techniques. Therefore, the rest of the study investigates the performance of GRIPMetal at various attack angles, leveraging flow and temperature field analyses to gain deeper insight into its thermal behavior.

5.1 Numerical Methods

5.1.1 Geometry and Orientation

A 3-dimensional view of a unit cell of the GRIPMetal array used in the simulations is shown in Fig. 23a, with the corresponding dimensions illustrated in Fig. 23(a,b). This geometry was created using the CAD software Solidworks, with the dimensions derived from statistical measurements of the array. In this study, a unit-cell was modeled in the spanwise direction, while multiple cells in the streamwise direction constituted the strip utilized for analysis. The performance of GRIPMetal was evaluated at five distinct α: 0°, 22.5°, 45°, 67.5°, and 90°, as depicted in Fig. 23(c-g).

For all attack angles, the hook-groove pair density was maintained constant at 36 pairs per strip. The width (W) of the strip was a function of α, and it varied to accommodate a unit-cell in the spanwise direction such that the geometry was fully periodic in the spanwise direction. Similarly, the strip length (L) was adjusted to maintain a constant hook-dimple pair density, leading to variations in the surface area (A_s) of the strips exposed to the flow. Overall, W, L, and A_s varied between 5.92 mm and 13.5 mm, 26.1 mm and 62.5 mm, and 464 mm^2 and 489 mm^2, respectively, as summarized in Table 5.

Table 5. Geometrical dimensions of the GRIPMetal strips at different α.

Parameter	Unit	Attack angle				
		$\alpha = 0°$	$\alpha = 22.5°$	$\alpha = 45°$	$\alpha = 67.5°$	$\alpha = 90°$
H^*	mm	1.5				
W	mm	5.92	13.5	8.77	13.5	6.48
L	mm	62.5	26.1	39.6	32.8	53.3

Table 5. Geometrical dimensions of the GRIPMetal strips at different α.

Parameter	Unit	Attack angle				
		$\alpha = 0°$	$\alpha = 22.5°$	$\alpha = 45°$	$\alpha = 67.5°$	$\alpha = 90°$
A_s	mm^2	489	488	467	466	464
A_o	mm^2	370	365	347	345	345

*H is constant at 1.5 mm for all cases in the present study, which is equal to the hook height.

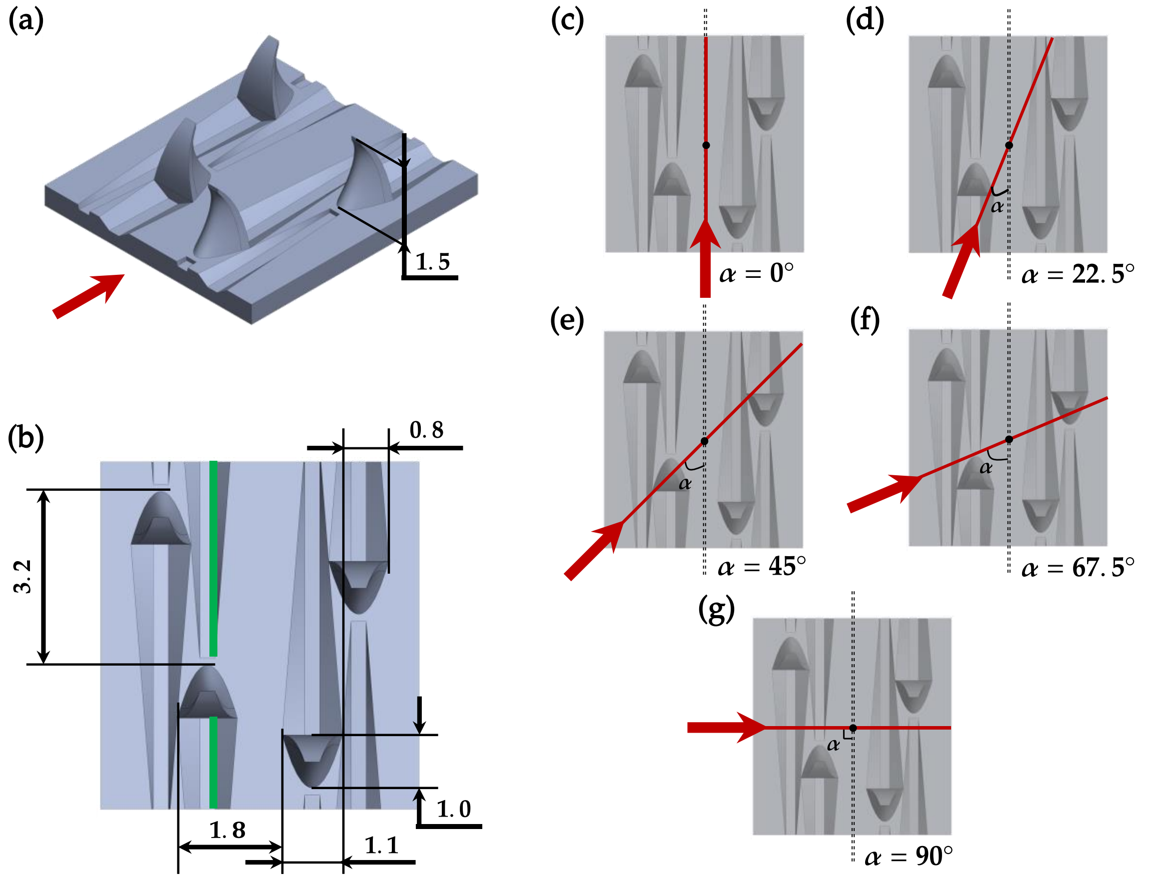

Fig. 23. A unit-cell of the GRIPMetal array used for the streamwise and spanwise directions: (a) isometric view and (b) plan view showing the geometrical dimensions of the array; array orientation at attack angle α = (c) 0° (streamwise), (d) 22.5°, (e) 45°, (f) 67.5°, and (g) 90° (spanwise). The groove length is the total length of the two lines highlighted in green and it measures 5.5 mm. All dimensions are in mm.

5.1.2 Numerical Setup and Boundary Conditions

The computational domain used in this study is illustrated in Fig. 24 and directly imitates the corresponding experimental setup described in 3.2. Water enters the test section through an entrance section, cools the array, then exits through the outlet section. Simulations were performed at ten different *Re*: 600, 800, 1000, 1200, 1400, 1600, 2000, 3000, 4000, and 5000. The water inlet velocity ranged from 0.1 m/s to 1.8 m/s to achieve the desired *Re*. The arrays were mounted on a copper block containing 4 cartridge heaters that provided heat to the computational domain.

The conjugate nature of the experimental setup adds complexity to the numerical modeling. Idealized thermal boundary conditions, such as those commonly used in numerical studies, may produce results that deviate from the real system. For example, replacing the copper block and four cartridge heaters with a uniform heat flux boundary condition at the bottom of the domain could yield surface temperatures that are more uniform than in the actual setup, leading to inaccurate Nu predictions, and consequently a misleading assessment of the thermal performance of the arrays. To ensure accuracy, the present numerical study is designed to closely emulate the experimental setup.

A uniform velocity profile was imposed at the inlet, and atmospheric pressure was specified at the outlet. Periodic boundary conditions were applied to both the left and right sides of the test section. A no-slip condition was imposed on the top wall of the flow channels as well as on the surfaces of the hooks and dimples. All external walls exposed to the surroundings were set to adiabatic boundaries.

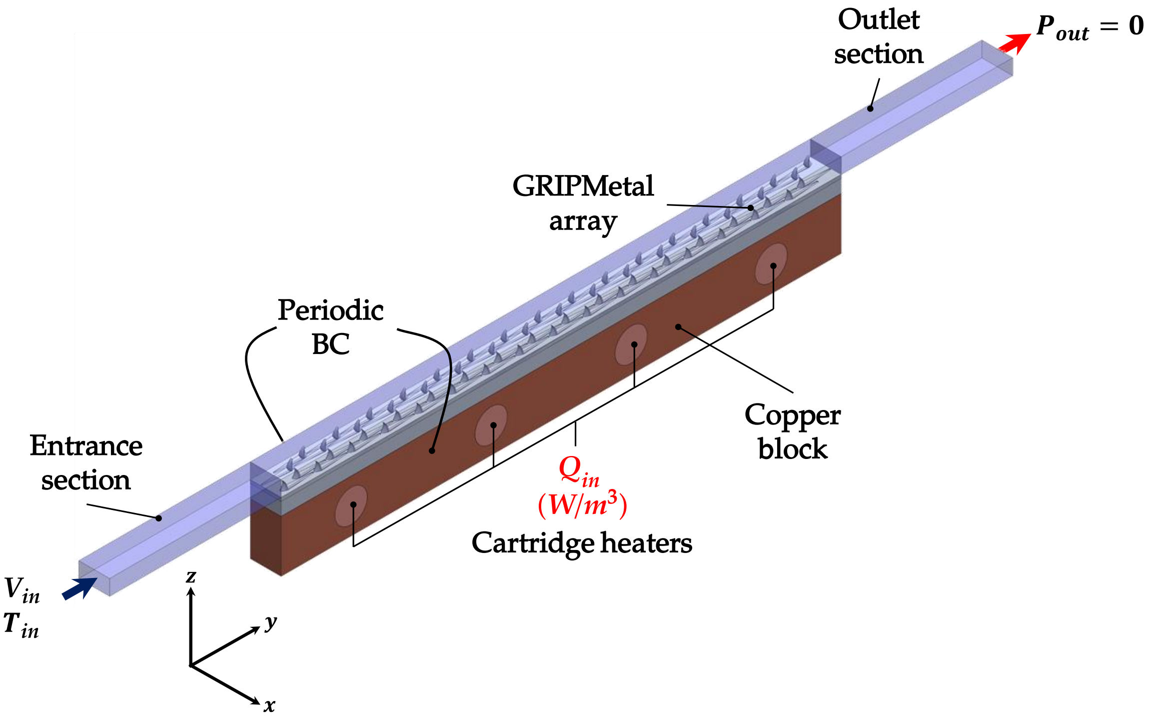

Fig. 24. Schematic of the computational domain for the GRIPMetal arrays. Length (L), width (W), and height (H) of the arrays are given in Table 5.

For model validation, a uniform volumetric heat generation rate ranging from 54 to 125 MW/m^3 was applied to the cartridge heaters to match the heater powers supplied during experimentation. The inlet temperature varied between 295 K and 297 K. For simulation involving different α, the copper block and cartridge heaters were removed to reduce computational costs. Instead, a uniform heat flux of 200 kW/m^2 was applied at the base of the GRIPMetal strip, while the inlet temperature was maintained at 295 K. Additionally, these simulations were conducted with the hooks fully shrouded inside the flow channel (H = 1.5 mm). This configuration corresponds to the condition that maximizes thermal enhancement, as deduced from the experimental results.

5.1.3 Governing Equations and Solution Methods

Heat transfer and flow fields were computed using conjugate three-dimensional flow simulations. The conjugate model used was steady, incompressible, and Newtonian, with constant fluid and solid thermophysical properties. Gravity effects and radiative heat transfer were neglected. The conjugate heat transfer problem was analyzed by numerically solving the continuity, momentum, and energy equations,

Continuity equation: $\boldsymbol{\nabla} \cdot \left(\rho_f \boldsymbol{V}\right) = 0$ (5.1)

Momentum equation:

$$\boldsymbol{V} \cdot \boldsymbol{\nabla}\left(\rho_f \boldsymbol{V}\right) = -\boldsymbol{\nabla} p + \boldsymbol{\nabla} \cdot (\mu \boldsymbol{\nabla} \boldsymbol{V}) \tag{5.2}$$

Fluid energy equation:

$$\boldsymbol{V} \cdot \boldsymbol{\nabla}\left(\rho_f C_{pf} T_f\right) = \boldsymbol{\nabla} \cdot (k_f \boldsymbol{\nabla} T_f) \tag{5.3}$$

Solid energy equation:

$$k_s \boldsymbol{\nabla}^2 T_s = \Phi \tag{5.4}$$

where $\boldsymbol{V}$ is the velocity vector, ρ is the density, p is the pressure, μ is the dynamic viscosity, C_p is the specific heat capacity, k is the thermal conductivity, and Φ is the volumetric heat generation rate, which is nonzero only during the validation stage. Subscripts f and s indicate fluid and solid domains, respectively.

Turbulence modeling was performed using the transition shear stress transport (Transition SST) model which augments the SST k-ω model – which combines the advantages of the k-ε and k-ω models via a blending function – by two additional transport equations for the intermittency and transition momentum thickness Re that describe transition and its onset in the flow [55]. The transport equations [56,57] of the Transition SST model are expressed as

Turbulent kinetic energy (k) equation:

$$\boldsymbol{\nabla} \cdot \left(\rho_f \boldsymbol{V} k\right) = \boldsymbol{\nabla} \cdot \left(\left(\mu + \frac{\mu_t}{\sigma_k}\right) \boldsymbol{\nabla} k\right) + \widehat{P}_k - \widehat{D}_k \tag{5.5}$$

Turbulent kinetic energy specific dissipation rate (ω) equation:

$$\boldsymbol{\nabla} \cdot \left(\rho_f \boldsymbol{V} \omega\right) = \boldsymbol{\nabla} \cdot \left(\left(\mu + \frac{\mu_t}{\sigma_\omega}\right) \boldsymbol{\nabla} \omega\right) + P_\omega - D_\omega + 2(1 - F_1) \frac{\rho \sigma_{\omega 2}}{\omega} \boldsymbol{\nabla} k \colon \boldsymbol{\nabla} \omega \tag{5.6}$$

Intermittency (γ) equation:

$$\boldsymbol{\nabla} \cdot \left(\rho_f \boldsymbol{V} \gamma\right) = \boldsymbol{\nabla} \cdot \left(\left(\mu + \frac{\mu_t}{\sigma_\gamma}\right) \boldsymbol{\nabla} \gamma\right) + P_\gamma - D_\gamma \tag{5.7}$$

Transition momentum thickness Re ($\widetilde{Re}_{\theta t}$) equation:

$$\boldsymbol{\nabla} \cdot \left(\rho_f \boldsymbol{V} \widetilde{Re}_{\theta t}\right) = \boldsymbol{\nabla} \cdot \left(\sigma_{\theta t} (\mu + \mu_t) \boldsymbol{\nabla} \widetilde{Re}_{\theta t}\right) + P_{\theta t} \tag{5.8}$$

The governing equations were discretized using the finite volume method and solved on ANSYS FLUENT 2022 R2. The default solver turbulence model constants were adopted except for C_{a1}, whose value was set to 4 in the present study (refer to [58] for details). Additionally, the default solver thermophysical properties for the solid and fluid domains were employed, except for the aluminum thermal conductivity, which was set to 167 W/mK in accordance with the value used during experimentation.

Pressure-velocity fields coupling was performed using the COUPLED scheme. Spatial discretization was performed using second order upwind schemes. Under-relaxation factors were 0.5 for momentum and pressure equations, while they were set to 0.5 for the energy equation. Simulations were considered converged when residuals dropped below 10^{-6} for the energy equation and 10^{-5} for the other equations. Alternatively, convergence was confirmed when no changes were observed in the energy and mass balances across the control volume, and steady readings were obtained from temperature and velocity point-monitors placed in both the fluid and solid domains.

5.1.4 Data Reduction

The thermal-hydraulic performance of the GRIPMetal arrays at different α was quantified via postprocessing the temperature, velocity, and pressure fields obtained from the simulations. The data reduction methodology outlined in sections 3.3 and 3.5 is applied to the numerical study, except for h_{avg} which was calculated as

$$h_{avg} = \frac{q_{flux} A_o}{A_s \Delta T_{LMTD}} \tag{5.9}$$

where q_{flux} is the uniform heat flux applied at the base of the strip, A_o is the strip base area (see Table 5), and ΔT_{LMTD} is the logarithmic mean temperature difference between the wall surface and the bulk fluid temperature, expressed as

$$\Delta T_{LMTD} = \frac{\left(T_{w,in} - T_{in}\right) - \left(T_{w,out} - T_{out}\right)}{ln\left(\frac{T_{w,in} - T_{in}}{T_{w,out} - T_{out}}\right)} \tag{5.10}$$

where $T_{w,in}$ and $T_{w,out}$ are the wall inlet and outlet temperatures, respectively, and T_{out} is the area-averaged water temperature at the outlet. The average Nusselt number, Nu_{avg}, was based on h, and the channel height H was kept constant at 1.5 mm for all cases. Additionally, the average coefficient of friction, f_{avg}, was calculated using Eq. (3.9).

The equivalent friction factor of the bare surface (f^*_o) required to evaluate the overall thermal performance (η_o) is expressed by the Shah and London [59] (Eq.(3.19)) and Petukhov [60] (Eq.(5.11)) correlations for $Re_o < 3000$ and $Re_o \geq 3000$, respectively.

$$f_o = (0.79\, ln\, Re_o - 1.64)^{-2} \tag{5.11}$$

Nu^*_o was evaluated at Re^*_o using Schmidt data [59] or the Gnielinski [61] correlation (Eq.(5.12)) for $Re_o < 3000$ and $Re_o \geq 3000$, respectively.

$$Nu_o = \frac{(f^*_o/8)(Re_o - 1000)Pr}{1 + 12.7(f^*_o/8)^{1/2}(Pr^{2/3} - 1)} \tag{5.12}$$

where f^*_o is evaluated from Eq.(5.11) and Pr is the flow's Prandtl number.

5.1.5 Grid Independence

A poly-hexahedral grid structure was generated on Fluent Meshing software. To ensure that the grid was sufficiently refined to accurately resolve the conjugate problem and produce reliable results, a mesh independence test was conducted. The test was performed for the critical case of the highest Re of 5000, $\alpha = 0°$, and for the scenario where 49.4% tip clearance was provided between the hooks and the wall. The test involved gradually reducing the maximum grid size in the computational domain and monitoring the relative changes in Nu_{avg} (ΔNu_{avg}) and f_{avg} (Δf_{avg}) with respect to the preceding larger grid size, as indicated in Table 6 and Fig. 25. Additionally, the number of inflation layers was gradually increased from 5 to 20 to ensure an adequately small y+ value for accurate near-wall resolution.

Table 6. Grid independence test for *Re* of 5000, $\alpha = 0°$, and 49.4% tip clearance.

Cell size*	Cell count	Nu_{avg}	$\lvert \Delta Nu_{avg} \rvert$	f_{avg}	$\lvert \Delta f_{avg} \rvert$
(mm)	(million)	(-)	(%)	(-)	(%)
2.05	0.0130	52.9	-	0.338	-
1.02	0.0705	56.9	7.6	0.381	13
0.512	0.393	59.3	4.2	0.380	0.029
0.256	3.97	56.0	5.4	0.385	1.3
0.128	8.85	55.7	0.7	0.386	0.23
0.0640	13.8	55.6	0.1	0.388	0.45

* Maximum cell size in the computational domain.

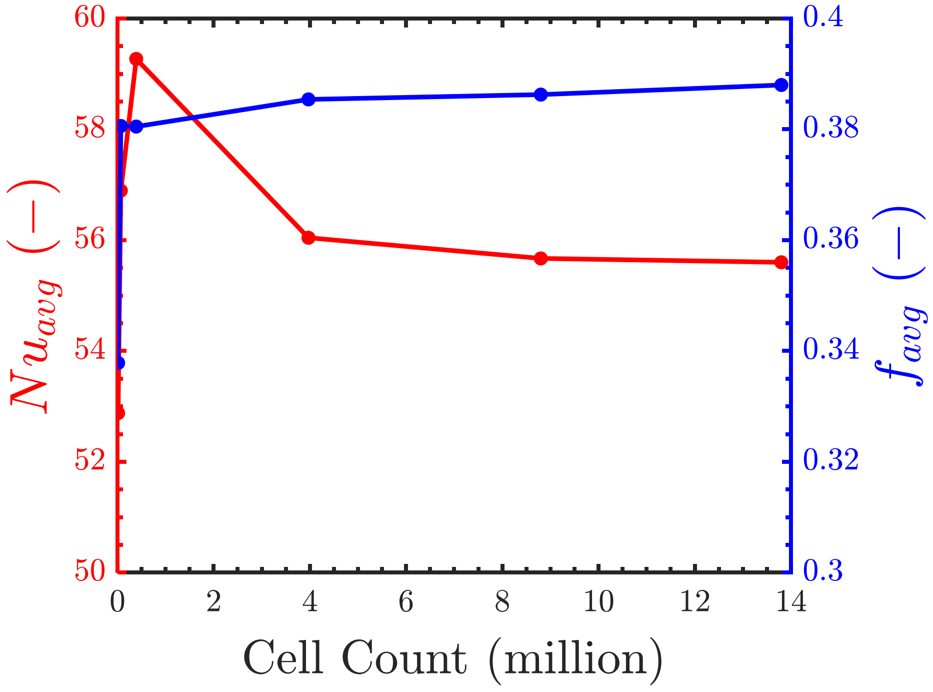

Fig. 25. Variation of Nu_{avg} and f_{avg} with the maximum cell size in the computational domain.

Table 6 shows that there was almost no change in Nu_{avg} or f_{avg} at a cell size of 0.0640 mm compared with the previous cell size, where ΔNu_{avg} and Δf_{avg} were within ±0.1% and ±0.45%, respectively. Therefore, this sufficiently refined grid size, resulting in 13.8M cells, was applied to all other cases.

5.1.6 Experimental Validation

Detailed experimental data reduction is described in section 3.3. It is identical to the numerical data reduction except for h_{avg}, which is computed as

$$h_{avg} = \frac{q_{flux}}{\Delta T_{avg}} \tag{5.13}$$

where ΔT_{avg} is the average difference between the surface temperature and the bulk fluid temperature, and it is calculated as

$$\Delta T_{avg} = T_{w,avg} - T_{bulk} \tag{5.14}$$

where $T_{w,avg}$ is the average wall temperature of the array, which is extrapolated from the RTDs readings via the one-dimensional Fourier's law of heat conduction, expressed as

$$T_{w,avg} = \frac{1}{4}\sum_{i=1}^{4} T_{RTD,i} - q_{flux}\frac{\delta}{k_{Al}} \tag{5.15}$$

where $T_{RTD,i}$ is the RTD reading and k_{Al} is the Al 6061 thermal conductivity, which is taken as 167 W/mK.

Table 1 shows a ±0.2 percent deviation in the hook height across the standard array, which leads to regions with 13.3% tip clearance when the arrays are assumed to be fully shrouded inside the channel. This deviation could result in significantly lower Nu_{avg} and f_{avg} than expected. To address the sensitivities of Nu_{avg} and f_{avg} to the presence of tip clearance, a numerical sensitivity analysis was conducted. In this analysis, the hook height was kept constant while tip clearance was introduced above the hooks by gradually increasing the channel height. The percentage variation in Nu_{avg} and f_{avg} was recorded in response to the percentage change in channel height, which corresponds to the tip clearance above the hooks. Based on the results of this sensitivity analysis, a 49.4% tip clearance case was chosen for the numerical model validation, as explained in section 5.2.1.

5.2 Numerical Results

5.2.1 Sensitivity Analysis and Experimental Validation

The variation of Nu_{avg} (ΔNu_{avg}) and f_{avg} (Δf_{avg}) with the channel tip clearance (C_{ch}) is shown in Fig. 26. A gradual decline is observed for both Nu_{avg} and f_{avg} with an increase in tip clearance, with the sensitivity being more pronounced for f_{avg}, as evidenced by the steeper negative slope. This behavior is attributed to the lower resistance to flow through the clearance. As a result, the flow velocity through the hooks decreases, leading to a lower convective heat transfer coefficient and a reduced pressure drop.

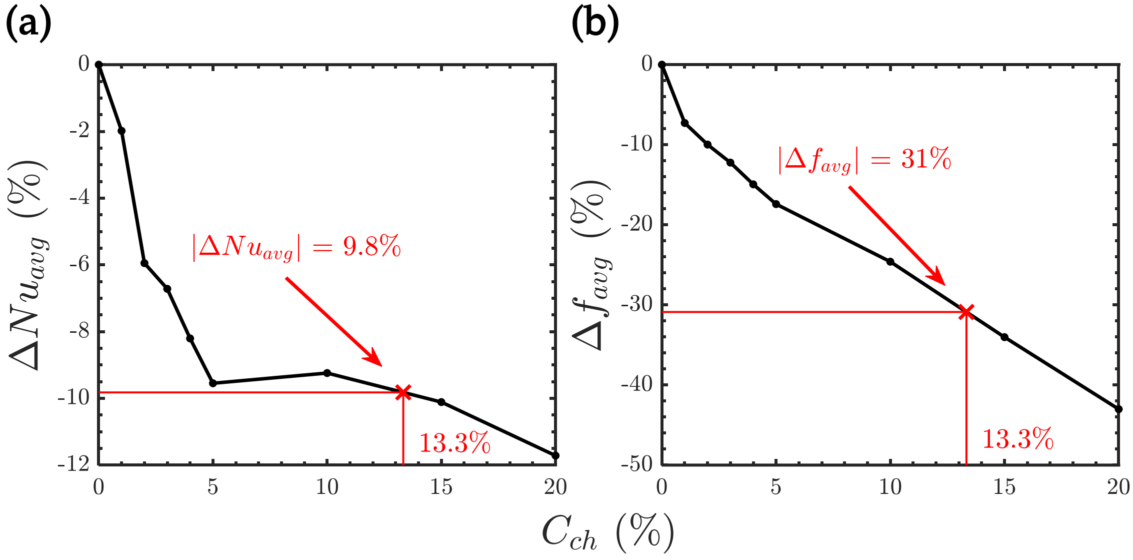

Fig. 26. Sensitivity of (a) Nu_{avg} and (b) f_{avg} to tip clearance for the GRIPMetal arrays.

As observed from Fig. 26, a 1% tip clearance reduces Nu_{avg} by 2% and f_{avg} by 7%. When the tip clearance increases to 20%, Nu_{avg} and f_{avg} decrease by nearly 12% and 43%, respectively. Although the reduction in thermal performance is not substantial, it is mildly beneficial for the hydraulic performance of the arrays, suggesting that a small tip clearance can be introduced to save pumping power without significantly affecting the thermal performance. Similar findings were reported by Reyes et al. [62] who noted that a 50% tip clearance resulted in only a 15% reduction in heat transfer through straight channels, while achieving a 50% reduction in pressure loss. It is also worth noting that a small 3% increase in thermal performance is observed when the tip clearance increases from 5% to 10%, a result that aligns with the findings of Moores and Joshi [52], who reported similar results when tip clearance increased from 6% to 12%. Furthermore, Mei et al. [34] highlighted that at certain tip clearances, accelerated flows are induced and the formation of recirculating wakes is reduced. These effects dominate the flow bypassing the pins, thereby improving heat transfer.

A 13.3% variation in the tip clearance across the GRIPMetal array may result in up to a 9.8% reduction in Nu_{avg} at certain locations, accompanied by a 31% decrease in f_{avg}, as illustrated in Fig. 26. While the deviation is not particularly significant for Nu_{avg}, it is quite notable for f_{avg}. This substantial sensitivity of f_{avg} to tip clearance emphasizes the importance of accurately accounting for such variations during model validation.

Due to this pronounced sensitivity and to avoid uncertainties during numerical validation, experimental results for the array with 49.4% tip clearance were employed to validate the numerical model, as presented in Fig. 27.

As shown in Fig. 27, the numerical model predictions closely match the experimental results, with both showing trends: a monotonic increase in Nu_{avg} and an exponential decrease in f_{avg} as Re increases. The maximum deviation in Nu_{avg} was 8.9% at Re = 5000, while the maximum deviation in f_{avg} was 8.4% at Re = 600, both relative to the mean experimental data. All numerical f_{avg} predictions were within the experimental uncertainties. For Nu_{avg}, the maximum deviation between the numerical results (outside the experimental uncertainty bounds) and the experimental data was 2.5%, after accounting for the uncertainty.

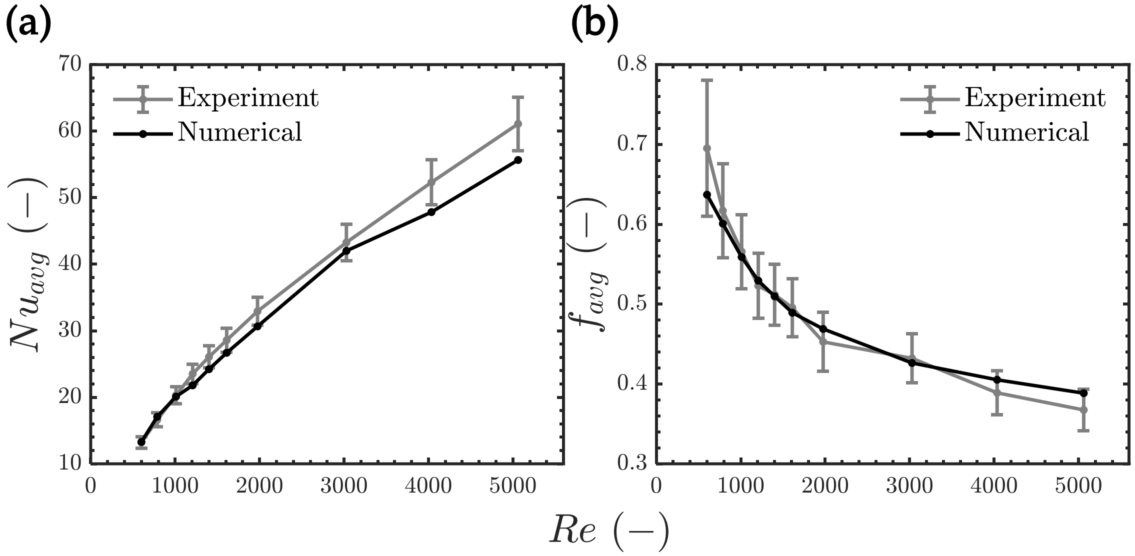

Fig. 27. Comparison between the numerical and experimental data for GRIPMetal with 49.4% tip clearance: (a) Nu_{avg} and (b) f_{avg}.

This excellent agreement between the numerical and experimental results validates the accuracy of the numerical setup, despite simplifying assumptions such as non-uniform hook height across the array, neglected surface roughness, and machining defects.

5.2.2 Effect of Attack Angle on the Thermal-hydraulic Performance

The influence of varying α on the thermo-hydraulic performance of GRIPMetal with the hooks fully shrouded inside the channel was examined, as shown in Fig. 28. Nu_{avg} exhibits a steep increase with increasing Re, while f_{avg} shows an exponential decrease with Re across all α.

For a given Re, Nu_{avg} is the lowest for α = 0°, then rises to a peak as α increases to 22.5°. Beyond 22.5°, Nu_{avg} decreases gradually as α increases to 67.5°, followed by a rise as α approaches 90°, as evident in Fig. 28c. An exception is observed at $Re = 600$, where Nu_{avg} for $\alpha = 0°$ is slightly higher than that for $\alpha = 67.5°$, as highlighted in Fig. 28a.

Relative to the baseline case of $\alpha = 0°$, the enhancement in Nu_{avg} varies significantly depending on α and Re. For $\alpha = 22.5°$, Nu_{avg} is enhanced by 26-44%, while for $\alpha = 45°$, the improvement is between 20 and 41%. At $\alpha = 90°$, the enhancement is slightly lower, between 3-38%. An outlier occurs $\alpha = 67.5°$ and $Re = 600$, where Nu_{avg} is 1% lower than the baseline case. Disregarding the lowest Re for $\alpha = 0°$, the enhancement in Nu_{avg} varies from 0.5% to 28%. At the highest Re, Nu_{avg} reaches 66, 64, 63, and 58 for $\alpha = 22.5°$, 45°, 90°, and 67.5°, respectively. These values represent improvements of 44%, 41%, 38%, and 28% compared with the baseline case.

The magnitudes of f_{avg} follow a similar pattern to Nu_{avg}, with $\alpha = 22.5°$ yielding the highest f_{avg}, followed by $\alpha = 45°$, $\alpha = 90°$, and $\alpha = 67.5°$ at the same Re, as indicated in Fig. 28d. An exception to this hierarchy occurs in the baseline case ($\alpha = 0°$), where f_{avg} is slightly higher than $\alpha = 45°$ but lower than $\alpha = 22.5°$. Consequently, only the $\alpha = 22.5°$ case yields a higher pressure drop penalty compared with the baseline, while all other angles result in a reduction in f_{avg}.

Depending on Re, the reduction in f_{avg} ranges from 1-3% for $\alpha = 45°$, 47-53% for $\alpha = 67.5°$, and 32-36% for $\alpha = 90°$, as depicted in Fig. 9c. In contrast, the penalization in f_{avg} is in the range of 15-20% for $\alpha = 22.5°$ relative to the baseline case. At $Re = 5000$, f_{avg} is 0.52, 0.28, and 0.34, for $\alpha = 45°$, $\alpha = 67.5°$, and $\alpha = 90°$, respectively, representing reductions of 1.6%, 48% and 35% compared with $\alpha = 0°$. Conversely, f_{avg} is 0.63 for $\alpha = 22.5°$, which is 18% higher than the baseline.

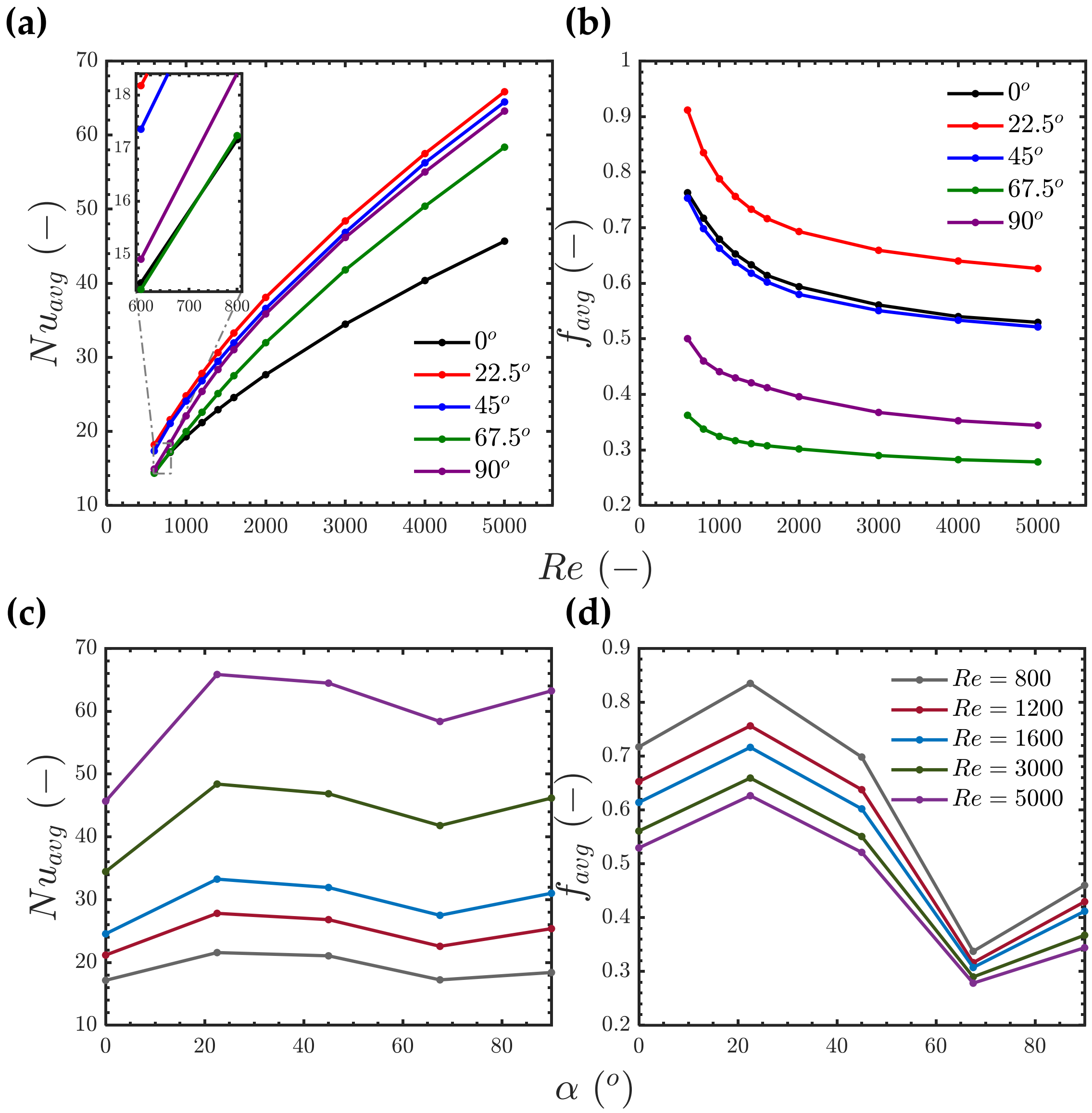

Fig. 28. Effect of *Re* on the thermo-hydraulic performance of GRIPMetal at zero tip clearance and several α: (a) Nu_{avg} and (b) f_{avg}. Effect of attack angle on the thermal-hydraulic performance of GRIPMetal arrays at different *Re*: (c) Nu_{avg} and (d) f_{avg}.

Attack angles like α = 45°, α = 67.5°, and α = 90° could serve as viable alternatives to the baseline case, offering the dual benefits of enhanced heat transfer and reduced flow resistance. This behavior has been recorded in the literature, where, for example, Abdelmohimen et al. [35] noted that α = 22.5°

resulted in a simultaneous improvement in thermal performance and a reduction in pumping power for staggered winged-pins.

5.2.3 Temperature and Flow Structure

The nature of local convection heat transfer mechanisms can be better understood by analyzing flow behavior and structures within the channel. Fig. 29-Fig. 32) present temperature contours, streamline maps, and turbulence intensity contours for the angles of attack with the best and worst heat transfer performance ($\alpha = 0°$ and $\alpha = 22.5°$, respectively) at $Re = 5000$, on a horizontal midplane in the flow domain x-y plane.

Temperature contours indicate that flow temperature increases as it progresses downstream through the arrays. Another notable observation is the correlation between high-velocity regions and low-temperature zones. Comparing Fig. 29a and Fig. 29b, the maximum flow temperature for $\alpha = 0°$ reaches 27.2^{o}C, which is significantly higher than the maximum of 25.2^{o}C observed for $\alpha = 22.5°$. However, the maximum velocity achieved for $\alpha = 0°$ is 4.4 m/s, slightly higher than 4.3 m/s for $\alpha = 22.5°$.

Fig. 30a shows substantial flow bypassing the hook features for $\alpha = 0°$, with a notable escape of fluid through the lateral sides due to reduced flow resistance in those areas. This results in significantly smaller flow velocities through the arrays compared with at the channel sides or the central spacing between the two hook sets. In contrast, the bypassing phenomenon is nearly absent in the $\alpha = 22.5°$ case, where the alignment of hooks ensures no continuous flow paths. Consequently, the flow is consistently redirected toward the hooks downstream after impinging upon the upstream hooks, as illustrated in Fig. 30b.

The higher velocity through the hooks for $\alpha = 22.5°$ enhances the convective heat transfer coefficient, thereby increasing Nu_{avg}. Therefore, even though the maximum velocity for $\alpha = 0°$ is slightly higher, the effective velocity through the hooks is lower, leading to a weaker cooling performance. Additionally, the bypassing flow in the $\alpha = 0°$ case results in a smaller pressure drop across the arrays compared with $\alpha = 22.5°$, where the flow encounters greater obstruction from the hooks.

Fig. 29 shows a significant difference in thermal boundary layer behavior between $\alpha = 0°$ and $\alpha = 22.5°$. For $\alpha = 0°$, the thermal boundary layer developing around each hook extends directly to the hook directly downstream. This results in a high temperature flow region remaining in contact with the hook surfaces, leading to lower heat transfer rates. In contrast, for $\alpha = 22.5°$, the flow in the wake of each hook mixes with the mainstream flow passing through the gaps before it impinges on the downstream hooks. This mixing process effectively cools the flow down, creating a higher temperature gradient between the flow and the hook surfaces which significantly increases the heat transfer rate for $\alpha = 22.5°$ compared with $\alpha = 0°$.

As illustrated by the streamlines in Fig. 30, flow separation occurs on both sides of the hooks, leading to elevated surface temperatures at the rear of the hooks compared with their front. This is due to the low velocity wake regions present there, which correspond to higher flow temperatures, as shown in Fig. 29. Vortices are generated in these wake regions downstream of the hooks, and their scale and magnitude significantly influence turbulence mixing and heat transfer enhancement.

For $\alpha = 22.5°$, the vortices are significantly larger than those for $\alpha = 0°$, resulting in higher turbulence intensity, as demonstrated in Fig. 31. The turbulence intensity peaks at 43% for $\alpha = 22.5°$, compared with 37% for $\alpha = 0°$. This intensified flow mixing contributes to lower flow temperatures and a higher temperature gradient between the array surface and the flow, thereby improving the heat transfer rate.

Additionally, the recirculation zones behind each hook for $\alpha = 0°$ are effectively trapped and isolated from the mainstream flow, limiting their contribution to heat transfer. Conversely, for $\alpha = 22.5°$, the recirculation zones are aligned at an angle relative to the flow direction, facilitating active advection with the mainstream flow causing an enhanced heat transfer, which is consistent with findings from previous studies [40,41,63].

The temperature and flow fields provide insight into the variation of the local Nusselt number (Nu_x) across the end walls of the array, which are shown in Fig. 32. Nu_x serves as an indicator of the surface temperature distribution, with lower Nu_x at the base compared with the hooks, highlighting the higher surface temperature of the base. The front and side surfaces of the hooks where the main flow impinges exhibit lower temperatures, as evident from the green contours covering a larger area upstream of the hooks. Downstream of the hooks, Nu_x remains elevated compared with regions without hooks. This is due to the wake flow promoting turbulence and enhancing convective heat transfer (see Fig. 31), an observation consistent with previous studies [64,65]. The regions of high Nu_x extend over a larger area for $\alpha = 22.5°$ compared with $\alpha = 0°$; the latter exhibits the lowest Nu_x values, particularly at the inlet and outlet of the array. This increased Nu_x for $\alpha = 22.5°$ explains an observed higher Nu_{avg} relative to $\alpha = 0°$.

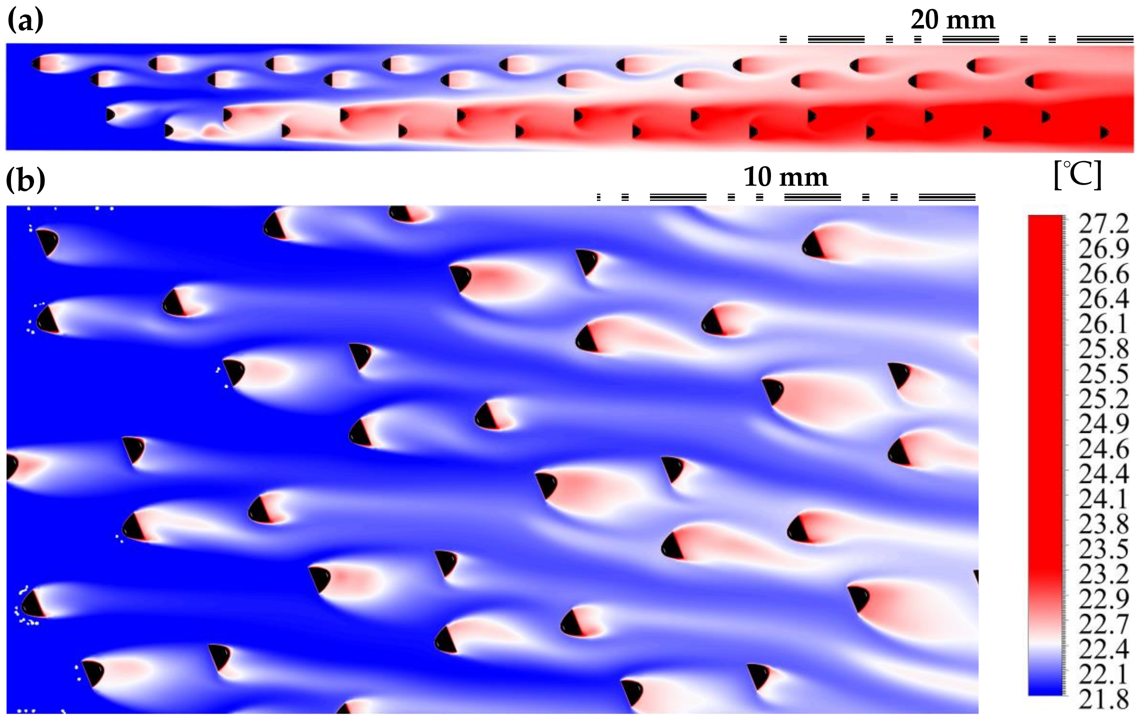

Fig. 29. Temperature contours for (a) $\alpha = 0°$ and (b) $\alpha = 22.5°$ at $Re = 5000$ on a midplane through the flow domain. Flow is from left to right.

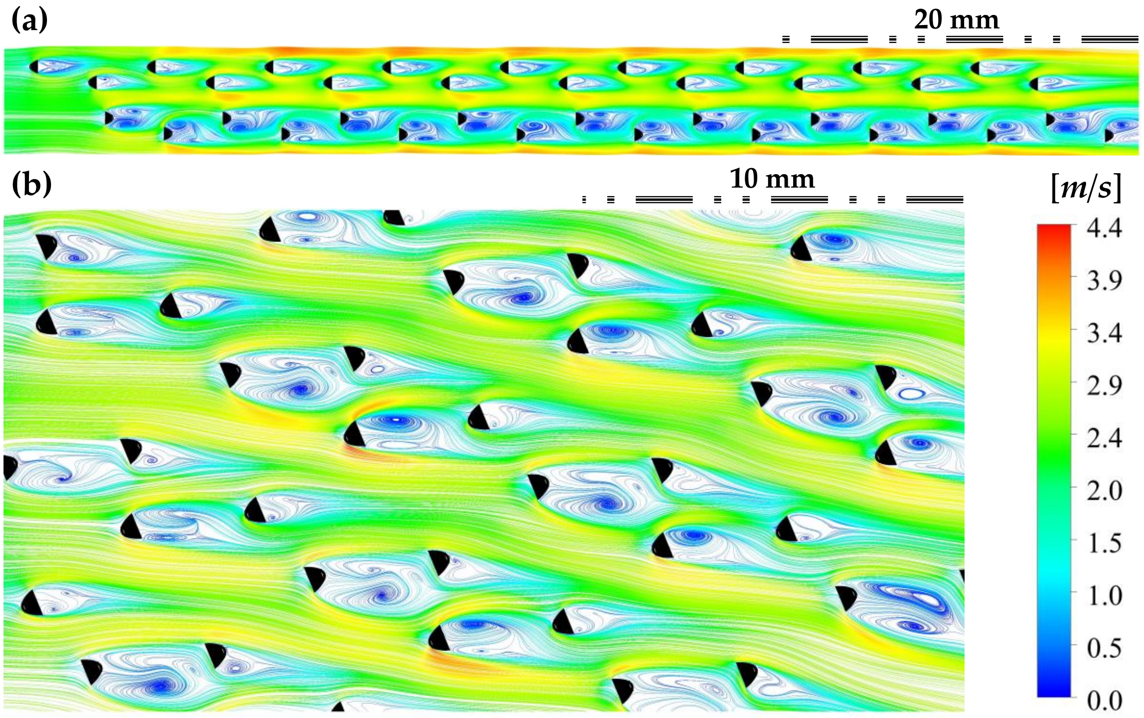

Fig. 30. Streamlines for (a) $\alpha = 0°$ and (b) $\alpha = 22.5°$ at $Re = 5000$ on a midplane through the flow domain. Flow is from left to right.

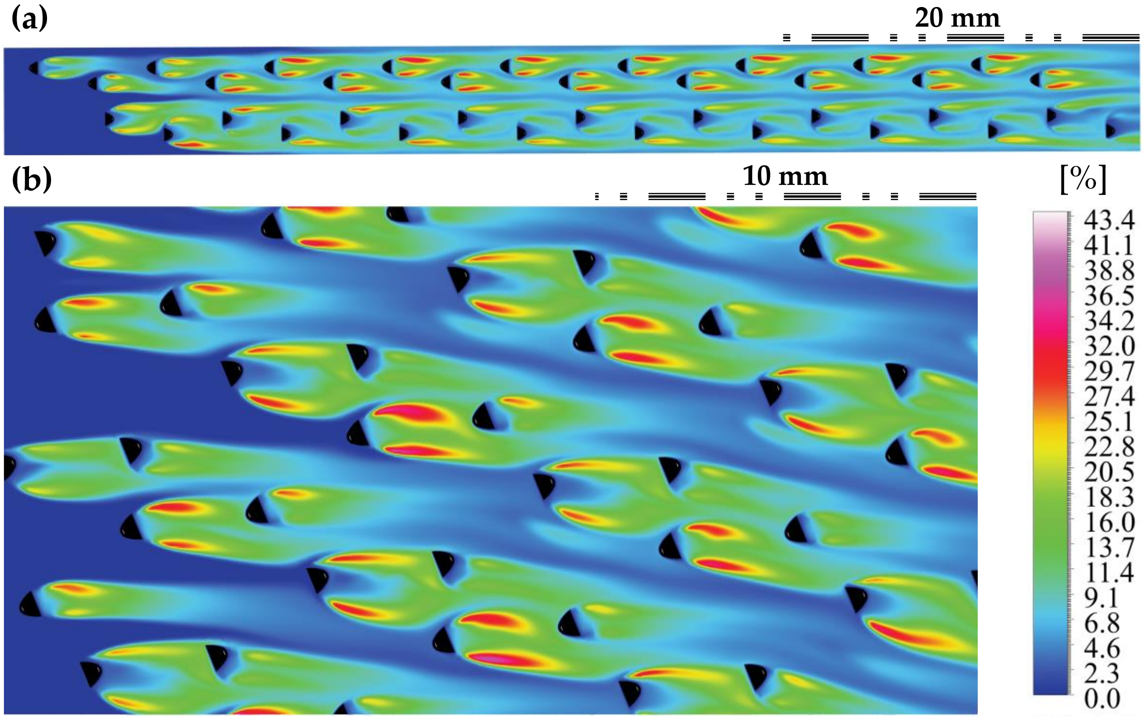

Fig. 31. Turbulence intensity contours for (a) α = 0° and (b) α = 22.5° at Re = 5000 on a midplane through the flow domain. Flow is from left to right.

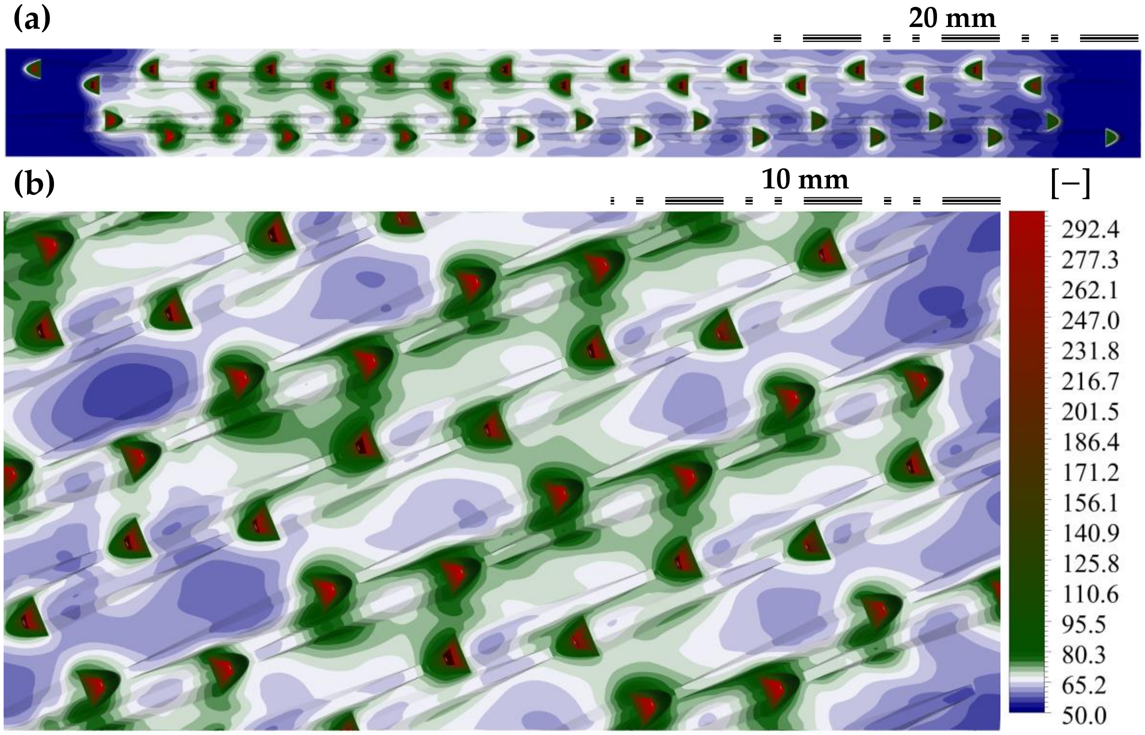

Fig. 32. Local Nusselt number contours for (a) α = 0° and (b) α = 22.5° at Re = 5000 on the array end-walls. Flow is from left to right.

5.2.4 Overall Thermal Performance at Different Attack Angles

The increase in Nu_{avg} and decrease in f_{avg} at various attack angles presents a promising alternative for enhancing thermal performance without requiring additional pumping power. To further illustrate the combined thermal-hydraulic performance of GRIPMetal, plots of η_o at different α are provided in Fig. 33.

All attack angles exhibit a declining asymptotic trend with increasing Re. Regardless of Re, the baseline case consistently demonstrates the lowest η_o, which ranges between 2.9 at $Re = 600$ and 0.46 at $Re = 5000$. In contrast, all other α result in higher η_o compared with the baseline case. Specifically, η_o ranges between 0.62 and 3.6 for $\alpha = 22.5°$, 0.65 and 3.5 for $\alpha = 45°$, 0.72 and 4.1 for $\alpha = 67.5°$, and 0.73 and 3.0 for $\alpha = 90°$. η_o increases with α, reaching a peak at 67.5° before decreasing at 90° or remaining relatively unchanged, as can be seen in Fig. 13b.

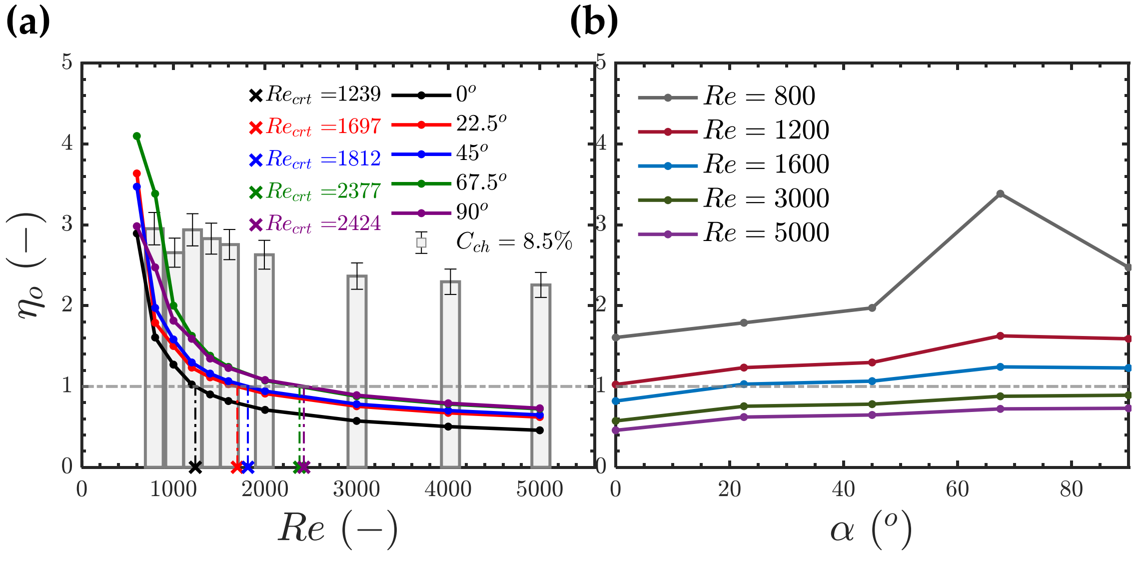

Fig. 33. Overall thermal performance of GRIPMetal at different attack angles: (a) variation of η_o with *Re* at several α (b) variation of η_o with α at several *Re*. The bars in (a) represent the experimental η_o obtained at $\alpha = 0°$ and 8.5% tip clearance.

Fig. 33a reveals that all attack angles maintain an η_o above one up to a critical Re (Re_{crt}) beyond which performance decline below 1. Re_{crt} is 1239, 1697, 1812, 2377, and 2424 for α = 0°, α = 22.5°, α = 45°, α = 67.5°, and α = 90°, respectively. This indicates that the overall performance of GRIPMetal becomes inferior to that of a bare surface once Re exceeds Re_{crt}. The decline in performance is attributed to the significantly high pressure drop across the arrays, causing the Re_o required to achieve the same pressure drop across the bare surface to be an order of magnitude higher than Re. Consequently, this high Re_o results in a Nu_o comparable to the Nu_{avg} of the arrays, leading to low η_o.

Fig. 33a also compares the performance of the array at different α with that of an array at 0° attack angle but with an 8.5% tip clearance. The data show that introducing a tip clearance significantly enhances the performance of GRIPMetal, and the performance improves with Re. Specifically, η_o is 84% and 393% higher for the 8.5% tip clearance case compared with the fully shrouded baseline case at Re = 800 and 5000, respectively. This trend is expected because Fig. 26 indicates that an 8.5% tip clearance leads to a 9.3% reduction in Nu_{avg} and a more substantial 22.4% reduction in f_{avg}. The significant drop in f_{avg} is the cause of the superior performance of the array with tip clearance, as shown in Fig. 33a.

These findings highlight the superior performance of GRIPMetal at flows below Re_{crt}. Beyond Re_{crt}, the performance of the arrays depends on the specific objective. Increasing α from 0° to 90° will gradually improve the overall thermal-hydraulic performance, but at the expense of high pumping power demands. If pumping power is not a limiting factor, then α = 22.5° would provide the highest thermal performance. Additionally, the results underscore that combining an optimized attack angle with a small tip clearance above the arrays can further enhance their overall performance.

Chapter 6

Summary, Conclusions, and Future Work

Arrays featuring hook-shaped fins and dimples (trademarked as GRIPMetal) were experimentally characterized to evaluate their thermal and hydraulic performance relative to a smooth, unfinned surface and surfaces with other enhancements. Additionally, their thermo-fluidic performance was numerically investigated under various attack angles ranging from 0° to 90°. The following conclusions are drawn from the findings:

- Heat transfer enhancement (Nu_{D_h}/Nu_o) peaked at $Re \approx 3{,}000$, and then gradually declined, reaching an asymptotic value as Re increased further.

- The hydraulic performance (f_{D_h}/f_o) increased rapidly at low *Re* and then stabilized at an asymptotic value as *Re* increased.

- At the same tip clearance, standard arrays showed the highest thermal enhancement, followed by heavy arrays, while mini arrays had the lowest Nu_{D_h}/Nu_o. As tip clearance increased, the performance of heavy arrays approached that of standard ones.

- Heavy and standard arrays exhibited nearly identical f_{D_h}/f_o at the same tip clearance, while the mini arrays had a slightly lower value.

- The overall efficiency (η_o) was highest at low *Re*, decreasing asymptotically as *Re* increased. At the same channel height, the standard arrays exhibited the highest performance, followed by the mini arrays, while the heavy arrays showed the lowest performance.

- The overall performance of the arrays improved as tip clearance increased, especially for mini arrays. Improvement was less pronounced for heavy arrays and depended on *Re* for standard arrays.

- Empirical correlations described Nu_h and f_h for the arrays with high accuracy, achieving a maximum rRMSE of 4.1% and 10%, respectively.

- The hydraulic performance of the arrays is very sensitive to the tip clearance above the hooks; a 20% tip clearance lowers the pressure drop by 43% while only reducing the thermal performance by 12%.

- Increasing α beyond the baseline case of 0° consistently enhances thermal performance. At Re = 5000, the lowest enhancement is 28% for α = 67.5°, while the highest is 44% at 22.5°.

- The hydraulic performance of the array generally surpasses the baseline case, with a maximum reduction in f_{avg} of 48% for α = 67.5° at Re = 5000. However, this does not hold for α = 22.5°, where f_{avg} increases by 18%.

- Arrays oriented at 45°, 67.5°, and 90° attack angles achieve a combined improvement in heat transfer and pressure drop reduction.

- Significant flow bypasses the features at α = 0° and results in a low thermal performance of the array configuration and minimizes pressure drop.

- The low temperature regions of the flow at α = 22.5° result in a larger temperature gradient between the hook surfaces and the flow, increasing the rate of heat transfer.

- When the arrays are fully shrouded, their overall performance remains above unity until an angle-dependent Re_{crt}, after which η_o falls below a bare surface, indicating the relatively higher pumping power required for GRIPMetal.

Overall, the GRIPMetal arrays demonstrated superior thermal-hydraulic performance compared with several heat enhancement techniques reported in the literature. Their relatively low-cost and robust manufacturing process positions them as promising alternatives to conventional heat transfer enhancement methods.

The enhanced thermal performance at $\alpha = 22.5°$ suggests the possibility of other intermediate α between 0° and 45° that could achieve higher Nu_{avg}. Additionally, the high thermal-hydraulic performance observed at $\alpha = 67.5°$ indicates a potential optimum angle between 45° and 90° that could maximize thermal performance while minimizing pumping power. These findings highlight the need for further investigation into intermediate α to optimize the performance of GRIPMetal in future research.

One limitation of this study is that the flow is not fully developed before entering the test section. A possible solution is to introduce an unheated entrance length before the heated section, which could be explored in future research. Additionally, future investigations should examine the effects of varying inter-fin spacings and modifying the primary geometrical features of the hooks and dimples. This includes exploring alternative tooling designs to enable the fabrication of diverse array geometries, including variations in feature patterns, spacings, and pitches. Understanding the influence of these parameters on the thermal and hydraulic behavior of the arrays is crucial for identifying optimal geometrical configurations that maximize performance. Additionally, research should Further analysis of local hook and dimple geometry – such as hook height, width, and other form factors – could provide deeper insight into convection enhancement mechanisms, uncovering new opportunities to improve the efficiency of GRIPMetal configurations.

References

[1] M.G. Mousa, Thermal performance of pin–fin heat sink subject in magnetic field inside rectangular channels, Exp Therm Fluid Sci 44 (2013) 138–146. https://doi.org/10.1016/J.EXPTHERMFLUSCI.2012.06.006.

[2] J.K. Ostanek, Improving pin-fin heat transfer predictions using artificial neural networks, J Turbomach 136 (2013). https://doi.org/10.1115/1.4025217/378221.

[3] F. Zhou, W. Zhou, C. Zhang, Q. Qiu, D. Yuan, X. Chu, Experimental and numerical studies on heat transfer enhancement of microchannel heat exchanger embedded with different shape micropillars, Appl Therm Eng 175 (2020) 115296. https://doi.org/10.1016/J.APPLTHERMALENG.2020.115296.

[4] C. Bi, G.H. Tang, W.Q. Tao, Heat transfer enhancement in mini-channel heat sinks with dimples and cylindrical grooves, Appl Therm Eng 55 (2013) 121–132. https://doi.org/10.1016/J.APPLTHERMALENG.2013.03.007.

[5] K. Bilen, U. Akyol, S. Yapici, Heat transfer and friction correlations and thermal performance analysis for a finned surface, Energy Convers Manag 42 (2001) 1071–1083. https://doi.org/10.1016/S0196-8904(00)00119-9.

[6] M. Eren, S. Caliskan, Effect of grooved pin-fins in a rectangular channel on heat transfer augmentation and friction factor using Taguchi method, Int J Heat Mass Transf 102 (2016) 1108–1122. https://doi.org/10.1016/J.IJHEATMASSTRANSFER.2016.07.005.

[7] K. Yeranee, Y. Rao, C. Xu, Y. Zhang, X. Su, Turbulent Flow Heat Transfer and Thermal Stress Improvement of Gas Turbine Blade Trailing Edge Cooling with Diamond-Type TPMS Structure, Aerospace 2024, Vol. 11, Page 37 11 (2023) 37. https://doi.org/10.3390/AEROSPACE11010037.

[8] S. Caliskan, Experimental investigation of heat transfer in a channel with new winglet-type vortex generators, Int J Heat Mass Transf 78 (2014) 604–614. https://doi.org/10.1016/J.IJHEATMASSTRANSFER.2014.07.043.

[9] M.K. Chyu, V. Natarajan, Heat transfer on the base surface of threedimensional protruding elements, Int J Heat Mass Transf 39 (1996) 2925–2935. https://doi.org/10.1016/0017-9310(95)00381-9.

[10] Y. Rao, C. Wan, Y. Xu, An experimental study of pressure loss and heat transfer in the pin fin-dimple channels with various dimple depths, Int J Heat Mass Transf 55 (2012) 6723–6733. https://doi.org/10.1016/J.IJHEATMASSTRANSFER.2012.06.081.

[11] G. Tanda, Heat transfer and pressure drop in a rectangular channel with diamond-shaped elements, Int J Heat Mass Transf 44 (2001) 3529–3541. https://doi.org/10.1016/S0017-9310(01)00018-7.

[12] R. Arbesman, Disc brake backing plate and method and apparatus of manufacturing same, 1997.

[13] A. Elkholy, J. Swift, R. Kempers, Hook-shaped structures to improve pool boiling heat transfer, Appl Therm Eng 219 (2023) 119665. https://doi.org/10.1016/J.APPLTHERMALENG.2022.119665.

[14] O. Khaled, J. Swift, R. Kempers, Thermal enhancement of rectangular channels using hook-shaped fins and dimples, Appl Therm Eng 217 (2022) 119272. https://doi.org/10.1016/J.APPLTHERMALENG.2022.119272.

[15] H.M. Ali, W. Arshad, Effect of channel angle of pin-fin heat sink on heat transfer performance using water based graphene nanoplatelets nanofluids, Int J Heat Mass Transf 106 (2017) 465–472. https://doi.org/10.1016/J.IJHEATMASSTRANSFER.2016.08.061.

[16] K.S. Yang, W.H. Chu, I.Y. Chen, C.C. Wang, A comparative study of the airside performance of heat sinks having pin fin configurations, Int J Heat Mass Transf 50 (2007) 4661–4667. https://doi.org/10.1016/J.IJHEATMASSTRANSFER.2007.03.006.

[17] D.E. Metzger, R.A. Berry, J.P. Bronson, Developing Heat Transfer in Rectangular Ducts With Staggered Arrays of Short Pin Fins, J Heat Transfer 104 (1982) 700–706. https://doi.org/10.1115/1.3245188.

[18] M.W. Alam, S. Bhattacharyya, B. Souayeh, K. Dey, F. Hammami, M. Rahimi-Gorji, R. Biswas, CPU heat sink cooling by triangular shape micro-pin-fin: Numerical study, International Communications in Heat and Mass Transfer 112 (2020) 104455. https://doi.org/10.1016/J.ICHEATMASSTRANSFER.2019.104455.

[19] Y. Rao, C. Wan, Y. Xu, S. Zang, Spatially-resolved heat transfer characteristics in channels with pin fin and pin fin-dimple arrays,

International Journal of Thermal Sciences 50 (2011) 2277–2289. https://doi.org/10.1016/J.IJTHERMALSCI.2011.06.013.

[20] Y. Xie, H. Qu, D. Zhang, Numerical investigation of flow and heat transfer in rectangular channel with teardrop dimple/protrusion, Int J Heat Mass Transf 84 (2015) 486–496. https://doi.org/10.1016/J.IJHEATMASSTRANSFER.2015.01.055.

[21] A. Shahsavar, M. Shahmohammadi, I.B. Askari, CFD simulation of the impact of tip clearance on the hydrothermal performance and entropy generation of a water-cooled pin-fin heat sink, International Communications in Heat and Mass Transfer 126 (2021) 105400. https://doi.org/10.1016/J.ICHEATMASSTRANSFER.2021.105400.

[22] K.A. Moores, J. Kim, Y.K. Joshi, Heat transfer and fluid flow in shrouded pin fin arrays with and without tip clearance, Int J Heat Mass Transf 52 (2009) 5978–5989. https://doi.org/10.1016/J.IJHEATMASSTRANSFER.2009.08.005.

[23] P. Bhandari, Y.K. Prajapati, Influences of tip clearance on flow and heat transfer characterstics of open type micro pin fin heat sink, International Journal of Thermal Sciences 179 (2022) 107714. https://doi.org/10.1016/J.IJTHERMALSCI.2022.107714.

[24] I.K. Choi, T. Kim, S.J. Song, T.J. Lu, Endwall heat transfer and fluid flow around an inclined short cylinder, Int J Heat Mass Transf 50 (2007) 919–930. https://doi.org/10.1016/J.IJHEATMASSTRANSFER.2006.08.012.

[25] M.K. Chyu, E.O. Oluyede, H.K. Moon, Heat Transfer on Convective Surfaces With Pin-Fins Mounted in Inclined Angles, Proceedings of

the ASME Turbo Expo 4 PART B (2009) 861–869. https://doi.org/10.1115/GT2007-28138.

[26] K. Takeishi, Y. Oda, Y. Miyake, Y. Motoda, Experimental and Numerical Study on the Convective Heat Transfer and Pressure Loss in Rectangular Ducts With Inclined Pin-Fin on a Wavy Endwall, Proceedings of the ASME Turbo Expo 4 (2013) 1061–1072. https://doi.org/10.1115/GT2012-69625.

[27] P. Narato, M. Wae-hayee, M.Z. Abdullah, C. Nuntadusit, Effect of pin inclination angle on flow and heat transfer characteristics for a row of pins in a flow channel, International Communications in Heat and Mass Transfer 110 (2020) 104396. https://doi.org/10.1016/J.ICHEATMASSTRANSFER.2019.104396.

[28] Q.X. Yang, Y.T. He, K.W. Song, Q.Z. Hou, Q. Zhang, X. Wu, Thermal performance improvement of a circular tube-and-fin heat exchanger by ellipsoidal protrusions on fin surfaces, International Journal of Thermal Sciences 196 (2024) 108746. https://doi.org/10.1016/J.IJTHERMALSCI.2023.108746.

[29] A. Lemouedda, M. Breuer, E. Franz, T. Botsch, A. Delgado, Optimization of the angle of attack of delta-winglet vortex generators in a plate-fin-and-tube heat exchanger, Int J Heat Mass Transf 53 (2010) 5386–5399. https://doi.org/10.1016/J.IJHEATMASSTRANSFER.2010.07.017.

[30] X. Zhang, Y. Wang, Z. Yu, D. Zhao, Numerical analysis of thermal-hydraulic characteristics on serrated fins with different attack angles

and wavelength to fin length ratio, Appl Therm Eng 91 (2015) 126–137. https://doi.org/10.1016/J.APPLTHERMALENG.2015.08.022.

[31] M.R. Haque, T.J. Hridi, M.M. Haque, CFD studies on thermal performance augmentation of heat sink using perforated twisted, and grooved pin fins, International Journal of Thermal Sciences 182 (2022) 107832. https://doi.org/10.1016/J.IJTHERMALSCI.2022.107832.

[32] E.M.S. El-Said, G.B. Abdelaziz, S.W. Sharshir, A.H. Elsheikh, A.M. Elsaid, Experimental investigation of the twist angle effects on thermo-hydraulic performance of a square and hexagonal pin fin array in forced convection, International Communications in Heat and Mass Transfer 126 (2021) 105374. https://doi.org/10.1016/J.ICHEATMASSTRANSFER.2021.105374.

[33] Y. Li, J. Zhang, Y. Zhang, J. Zhang, J. Wei, S. Ma, B. Sunden, G. Xie, Effect of square pin-fin twist on thermo-hydraulic performance of a rectangular channel in forced convection, International Communications in Heat and Mass Transfer 157 (2024) 107824. https://doi.org/10.1016/J.ICHEATMASSTRANSFER.2024.107824.

[34] D. Mei, X. Lou, M. Qian, Z. Yao, L. Liang, Z. Chen, Effect of tip clearance on the heat transfer and pressure drop performance in the micro-reactor with micro-pin–fin arrays at low Reynolds number, Int J Heat Mass Transf 70 (2014) 709–718. https://doi.org/10.1016/J.IJHEATMASSTRANSFER.2013.11.060.

[35] M.A.H. Abdelmohimen, M.A. Hussien, S. Algarni, M.A. Karali, C. Ahamed Saleel, G.M.S. Ahmed, H.A. Refaey, Numerical investigation of thermal performance enhancement of pin fin heat sink using wings

with different angles, Ain Shams Engineering Journal 15 (2024) 102584. https://doi.org/10.1016/J.ASEJ.2023.102584.

[36] J.Y. Ho, K.K. Wong, K.C. Leong, T.N. Wong, Convective heat transfer performance of airfoil heat sinks fabricated by selective laser melting, International Journal of Thermal Sciences 114 (2017) 213–228. https://doi.org/10.1016/J.IJTHERMALSCI.2016.12.016.

[37] S. Acharya, Thermo-fluidic analysis of microchannel heat sink with inline/staggered square/elliptical fins, International Communications in Heat and Mass Transfer 147 (2023) 106961. https://doi.org/10.1016/J.ICHEATMASSTRANSFER.2023.106961.

[38] M. Pallikonda, K.K. Kupireddi, K. Balasubramanian, V.P. Chandramohan, P.S. Lee, C.C. Kong, Heat transfer enhancement using elliptical fin microchannel, Asia-Pacific Journal of Chemical Engineering 16 (2021) e2712. https://doi.org/10.1002/APJ.2712.

[39] Y.J. Lee, P.K. Singh, P.S. Lee, Fluid flow and heat transfer investigations on enhanced microchannel heat sink using oblique fins with parametric study, Int J Heat Mass Transf 81 (2015) 325–336. https://doi.org/10.1016/J.IJHEATMASSTRANSFER.2014.10.018.

[40] H. Sallar, M. Irfan, M.M. Khan, M.W. Shahzad, Hydro-thermal performance of an I-shaped pin fin microchannel heat sink with variable pin fin height, thickness and orientation, International Communications in Heat and Mass Transfer 160 (2025) 108256. https://doi.org/10.1016/J.ICHEATMASSTRANSFER.2024.108256.

[41] P. Kangude, P.S. Kumavat, E. Shatskiy, A.J. Robinson, Numerical investigation of tip clearance designs for oblique-cut fin

microchannels, Appl Therm Eng 257 (2024) 124415. https://doi.org/10.1016/J.APPLTHERMALENG.2024.124415.

[42] R.L. Webb, E.R.G. Eckert, Application of rough surfaces to heat exchanger design, Int J Heat Mass Transf 15 (1972) 1647–1658. https://doi.org/10.1016/0017-9310(72)90095-6.

[43] R. Karwa, C. Sharma, N. Karwa, Performance Evaluation Criterion at Equal Pumping Power for Enhanced Performance Heat Transfer Surfaces, Journal of Solar Energy 2013 (2013) 1–9. https://doi.org/10.1155/2013/370823.

[44] R.K. Shah, A.L. London, Laminar flow forced convection in ducts: a source book for compact heat exchanger analytical data, Academic press, 2014.

[45] W. Nusselt, Der Wärmeaustausch zwischen Wand und Wasser im Rohr, Forschung Auf Dem Gebiete Des Ingenieurwesens 2 (1931) 309–313. https://doi.org/10.1007/BF02583210/METRICS.

[46] M.N. Ozisik, Heat transfer: a basic approach, McGraw-Hill New York, 1985.

[47] O.G. Jones, An Improvement in the Calculation of Turbulent Friction in Rectangular Ducts, J Fluids Eng 98 (1976) 173–180. https://doi.org/10.1115/1.3448250.

[48] KLINE S. J., Describing Uncertainties in Single-Sample Experiments, Mech. Eng. 75 (1963) 3–8. https://cir.nii.ac.jp/crid/1572261549103675008.bib?lang=en (accessed September 12, 2023).

[49] F.W. Dittus, Heat transfer in automobile radiators of the tubular type, Univ. of California Pub., Eng. 2 (1930) 443–461.

[50] B.A. Jubran, M.A. Hamdan, R.M. Abdualh, Enhanced heat transfer, missing pin, and optimization for cylindrical pin fin arrays, (1993).

[51] B. Sahin, A. Demir, Thermal performance analysis and optimum design parameters of heat exchanger having perforated pin fins, Energy Convers Manag 49 (2008) 1684–1695. https://doi.org/10.1016/J.ENCONMAN.2007.11.002.

[52] K.A. Moores, Y.K. Joshi, Effect of Tip Clearance on the Thermal and Hydrodynamic Performance of a Shrouded Pin Fin Array, J Heat Transfer 125 (2003) 999–1006. https://doi.org/10.1115/1.1621897.

[53] M.K. Chyu, C.H. Yen, W. Ma, T.I.P. Shih, Effects of Flow Gap Atop Pin Elements on the Heat Transfer From Pin Fin Arrays, Proceedings of the ASME Turbo Expo 3 (2014). https://doi.org/10.1115/99-GT-047.

[54] H. Sun, H. Fu, H. Ma, T. Sun, Y. Luan, P. Zunino, Heat transfer enhancement mechanism of elliptical cylinder for minichannels with delta winglet longitudinal vortex generators, International Journal of Thermal Sciences 198 (2024) 108839. https://doi.org/10.1016/J.IJTHERMALSCI.2023.108839.

[55] M. Bahiraei, N. Mazaheri, M.R. Daneshyar, Employing elliptical pin-fins and nanofluid within a heat sink for cooling of electronic chips regarding energy efficiency perspective, Appl Therm Eng 183 (2021) 116159. https://doi.org/10.1016/J.APPLTHERMALENG.2020.116159.

[56] F.R. Menter, R. Langtry, S. Völker, Transition Modelling for General Purpose CFD Codes, Flow Turbul Combust 77 (2006) 277–303. https://doi.org/10.1007/S10494-006-9047-1/METRICS.

[57] F.R. Menter, Two-equation eddy-viscosity turbulence models for engineering applications, AIAA Journal 32 (1994) 1598–1605. https://doi.org/10.2514/3.12149.

[58] A. Fluent, Ansys fluent theory guide, Ansys Inc., USA 15317 (2011) 724–746.

[59] R.K. Shah, A.L. London, Rectangular Ducts, Laminar Flow Forced Convection in Ducts (1978) 196–222. https://doi.org/10.1016/B978-0-12-020051-1.50012-7.

[60] B.S. Petukhov, Heat Transfer and Friction in Turbulent Pipe Flow with Variable Physical Properties, Adv Heat Transf 6 (1970) 503–564. https://doi.org/10.1016/S0065-2717(08)70153-9.

[61] V. Gnielinski, New equations for heat and mass transfer in the turbulent flow in pipes and channels, NASA STI/Recon Technical Report A 41 (1975) 8–16.

[62] M. Reyes, J.R. Arias, A. Velazquez, J.M. Vega, Experimental study of heat transfer and pressure drop in micro-channel based heat sinks with tip clearance, Appl Therm Eng 31 (2011) 887–893. https://doi.org/10.1016/J.APPLTHERMALENG.2010.11.011.

[63] A. Renfer, M.K. Tiwari, R. Tiwari, F. Alfieri, T. Brunschwiler, B. Michel, D. Poulikakos, Microvortex-enhanced heat transfer in 3D-integrated liquid cooling of electronic chip stacks, Int J Heat Mass

Transf 65 (2013) 33–43. https://doi.org/10.1016/J.IJHEATMASSTRANSFER.2013.05.066.

[64] P. Singh, J. Pandit, S. V. Ekkad, Characterization of heat transfer enhancement and frictional losses in a two-pass square duct featuring unique combinations of rib turbulators and cylindrical dimples, Int J Heat Mass Transf 106 (2017) 629–647. https://doi.org/10.1016/J.IJHEATMASSTRANSFER.2016.09.037.

[65] S.A. Lawson, A.A. Thrift, K.A. Thole, A. Kohli, Heat transfer from multiple row arrays of low aspect ratio pin fins, Int J Heat Mass Transf 54 (2011) 4099–4109. https://doi.org/10.1016/J.IJHEATMASSTRANSFER.2011.04.001.